# Remote Sensing Estimates of Time-Resolved HONO and NO₂ Emission Rates and Lifetimes in Wildfires

Carley D. Fredrickson[1†], Scott J. Janz[2], Lok N. Lamsal[2,3], Ursula A. Jongebloed[1], Joshua L. Laughner[4], Joel A. Thornton[1]

[1]Department of Atmospheric and Climate Science, University of Washington, Seattle, Washington 98195, United States
[2]NASA Goddard Space Flight Center, Greenbelt, Maryland 20771, United States
[3]Goddard Earth Sciences Technology and Research, University of Maryland, Baltimore County, Baltimore, Maryland, 21228, United States
[4]Jet Propulsion Laboratory, California Institute of Technology, Pasadena, California, 91109, United States

[†]Now at Ramboll Americas Engineering Solutions, Inc., Seattle, Washington 98164, United States

*Correspondence to*: Joel A. Thornton (joelt@uw.edu)

**Abstract.** Quantification of wildfire emissions is essential for comprehending and simulating the effects of wildfires on atmospheric chemical composition. Sub-orbital measurements of vertical column nitrous acid (HONO) and nitrogen dioxide (NO₂) were made during the Fire Influence on Regional to Global Environments and Air Quality (FIREX-AQ) field campaign using the GeoCAPE Airborne Simulator (GCAS) instrument aboard the NASA ER-2 aircraft. Emission rates and lifetimes of HONO and NO₂ from the Sheridan Fire were estimated by fitting exponentially modified Gaussians (EMGs) to line densities, a technique previously used to estimate urban and point source NO₂ emissions. As the EMG approach does not capture temporal changes in emissions and lifetimes due to time-varying fire behavior, we developed a Monte Carlo implementation of the Python Editable Chemical Atmospheric Numeric Solver (PECANS) model that includes diurnal fire radiative power (FRP) behavior. We assess the validity of a range of emission rate and lifetime combinations for both HONO and NO₂ as the fire evolves by comparing the resulting line density predictions to the observations. We find that our method results in emissions that are lower than top-down biomass burning emissions inventories and higher than bottom-up inventories. Our approach is applicable to interpreting time-resolved remotely sensed measurements of atmospheric trace gases such as those now becoming available with instruments aboard geo-stationary satellites such as the Tropospheric Emissions: Monitoring of Pollution (TEMPO) and the Geostationary Environment Monitoring Spectrometer (GEMS) instruments.

## 1 Introduction

Wildfires pose several risks to infrastructure, air quality, and climate. Wildfires emit particulate matter, reduced and oxidized nitrogen, carbon monoxide, and volatile organic compounds (VOCs) that degrade local and regional air quality and impact human health (Akagi et al., 2011; Andreae, 2019). The reactions of the compounds found in wildfire smoke additionally lead

to the creation of ozone and other hazardous air pollutants (Buysse et al., 2019; Jaffe and Wigder, 2012). The impact of wildfires can even extend past the troposphere, where pyrocumulonimbus clouds formed from wildfires can inject smoke particles into the stratosphere, enhancing chlorine activation and stratospheric ozone depletion, as well as surface cooling
35 and stratospheric heating (Bernath et al., 2022; Solomon et al., 2022, 2023; Ye et al., 2021). As the intensity of fires and burned area from fires are predicted to increase in the United States in the future, it is important to understand how wildfire emissions change with fire properties and how these emissions impact local, regional, and global atmospheric composition.

There are two distinct approaches for estimating global fire emissions within biomass burning emission inventories: (1) a
40 bottom-up approach that uses burned area as a proxy for amount of material burned and (2) a top-down approach that uses fire radiative power (FRP) as a proxy for amount of material burned. Some examples of burned area inventories are the Global Fire Emissions Database (GFED) and the Fire INventory from NCAR (FINN) (Giglio et al., 2013; Wiedinmyer et al., 2011). Some examples of FRP-derived inventories are the Quick Fire Emissions Dataset (QFED) and the Global Fire Assimilation System (GFAS) (Darmenov and da Silva, 2015; Kaiser et al., 2012). Both approaches ultimately rely on
45 emission factors, which translate the biomass burned to the emitted mass of species constrained by *in situ* or remotely sensed observations. The amount of biomass burned is tied to satellite-measured surface properties, but fire emissions can also be estimated by measuring a fire's smoke plume within the atmosphere. While historically used to measure the emissions and lifetimes of urban pollution (Goldberg et al., 2019; Laughner and Cohen, 2019), the exponentially modified Gaussian (EMG) approach has also been applied to wildfire smoke plumes detected by polar-orbiting satellites, making observations typically
50 once a day (Griffin et al., 2021; Jin et al., 2021). Forming conclusions using daily observations of fires, while a good starting point, does not capture the diurnal variability that fires exhibit (Wiggins et al., 2020). With the emergence of geostationary satellites reporting atmospheric composition, our understanding of the diurnal emissions of wildfires and the extent of their variability will be vastly improved.

55 Recent advances in remote sensing and *in situ* observations have enabled improved assessments of wildfire emissions of reactive nitrogen. $NO_2$ is routinely measured by satellites and by air quality monitors and these observations have been used extensively to estimate $NO_x$ ($NO_x$ = NO + $NO_2$) emissions from anthropogenic and, more recently, wildfire sources. However, most fire emission inventories do not include the reactive nitrogen compound nitrous acid (HONO), even though HONO was found to contribute at least 50% of a smoke plume's hydroxyl radicals (OH) for hours downwind of the fire
60 (Peng et al., 2020; Theys et al., 2020). HONO has the greatest relevance in the youngest parts of a smoke plume, where its rapid photooxidation (10–15 min lifetime at solar noon) generates OH, especially on plume edges (Decker et al., 2021; Palm et al., 2021; Wang et al., 2021). Thus, excluding HONO in fire emissions can greatly impact estimates of the initial chemical evolution of a smoke plume and generation of ozone and secondary organic aerosol (Wolfe et al., 2022).

65    After $NO_x$ is emitted, there are multiple pathways that can remove $NO_x$ from a smoke plume. $NO_2$ can react with oxidized acetaldehyde to form peroxyacetyl nitrate (PAN), a temporary reservoir species that breaks down in warmer temperatures and acts as a source of $NO_x$ downwind of a fire. $NO_x$ can also react with other radical species to form $RO_2NO_2$, $RONO_2$, $HNO_3$, $HO_2NO_2$, particulate nitrates, gas-phase organic nitrogen, nitrogen-containing VOCs and nitroaromatics. A number of studies have quantified the lifetime of $NO_x$ within wildfire smoke, under a variety of conditions, with estimates ranging

70    from 20 minutes to 11 hours (Adams et al., 2019; Akagi et al., 2012; Berezin et al., 2016; Griffin et al., 2021; Jin et al., 2021; Juncosa Calahorrano et al., 2021a; Takegawa et al., 2003; Wolfe et al., 2022).

   In this study, we provide new remotely sensed measurements of vertical column HONO and $NO_2$ from the Sheridan Fire in the Prescott National Forest, Arizona taken roughly every 20 minutes over the course of the fire's activity on 16 August

75    2019. Additionally, we make estimates of the Sheridan Fire's emission rates and smoke plume effective lifetimes for every observation during its evolution. These measurements were made using the GeoCAPE Airborne Simulator (GCAS) instrument aboard the National Aeronautics and Space Administration (NASA) ER-2 aircraft for the Fire Influence on Regional to Global Environments and Air Quality (FIREX-AQ) campaign. We use a simple one-dimensional (1-D) horizontal model to evaluate the assumptions within and the accuracy of the EMG approach on wildfire smoke plumes. To

80    improve upon the EMG approach, we provide a new emission rate and lifetime methodology using Monte Carlo 1-D model simulations and the diurnal FRP from geostationary satellites to derive emission rates and lifetimes for HONO and $NO_2$, using the Sheridan Fire as a test case.

## 2 Data and methods

### 2.1 FIREX-AQ

85    During the summer of 2019, a collaborative, multi-agency campaign called the Fire Influence on Regional to Global Environments and Air Quality (FIREX-AQ) studied wildfires and agricultural fires in the continental United States to assess fires' impact on air quality and climate. One of FIREX-AQ's measurement platforms was the NASA ER-2 high-altitude measurement aircraft. On the ER-2, the GeoCAPE Airborne Simulator (GCAS) instrument remotely retrieved $NO_2$ and HONO vertical column densities. The GCAS instrument is composed of two push-broom spectrometers: the first records the

90    spectrum as absolute nadir radiance in the ultraviolet to visible (UV-Vis), from 300 to 490 nm, and the second records the spectrum in the visible to near-infrared (Vis-NIR) from 480 to 900 nm (Kowalewski and Janz, 2014). The UV-Vis window has a spectral resolution of 0.6 nm with uncertainty in $NO_2$ slant column retrievals close to $0.8 \times 10^{15}$ molec cm$^{-2}$ (Judd et al., 2020). The GCAS instrument shares similar design specifications with the TROPOMI and TEMPO instruments. As flown on the ER-2 for FIREX-AQ, the GCAS data has a horizontal resolution of 500 m.

95

Atmospheric
Measurement
Techniques
Discussions

The retrieval method for GCAS measurements includes the differential optical absorption spectroscopy (DOAS) spectral fitting that yields slant column densities (SCDs) (Plane and Saiz-Lopez, 2006; Platt and Stutz, 2008). By fitting the differential cross-sections of trace gases to the measured differential absorption spectra, the trace gas concentrations along the light path can be determined via the Beer-Lambert law. The log-normalized GCAS spectra were fit to cross-section data

100 using the software package QDOAS developed at the Belgian Institute for Space Aeronomy (BIRA-IASB) (https://uv-vis.aeronomie.be/software/QDOAS/index.php). The fitting windows for $NO_2$ and HONO are 425 to 460 nm and 345 to 390 nm, respectively.

A compound's SCD is transformed to a vertical column density (VCD) by dividing the SCD by an air mass factor (AMF).

105 An AMF is a wavelength- and altitude-dependent quantity representing the effect that the light's path has on retrieval. An AMF depends on observation geometry, surface reflectivity, a-priori vertical profiles, aerosols, and other factors that affect the measurement sensitivity. In this study, AMFs are calculated using the vector linearized discrete ordinate radiative transfer code (VLIDORT). This radiative transfer code is a multiple-scattering model calculating radiances and weighting functions in a multilayer atmosphere. The AMFs for HONO and $NO_2$ are derived similarly to the procedure in Lamsal et al.

110 (2017), where AMFs are calculated using non-Lambertian bidirectional reflectance distribution functions (Lamsal et al., 2017). A-priori profiles are taken from the NASA GEOS GMI simulation at 0.25 deg x 0.25 deg resolution. Given the complex radiative transfer through evolving wildfire plumes, the VCD used here may carry significant uncertainties. However, our conclusions are focused mostly upon the comparisons of emissions and lifetime estimates, and less so on the absolute values of each trace gas. That said, we do provide comparisons of these quantities to emission inventories and

115 model estimates of chemical lifetime together with a discussion of the associated uncertainties in Sections 3.3 and 3.4.

The ER-2 aircraft performed 10 flights between 2 August and 21 August 2019. In this work, we present observations from the Sheridan Fire. The Sheridan Fire was ignited by lightning on 5 August 2019 in Arizona's Prescott National Forest and continued to burn throughout the campaign. On 16 August 2019, the Sheridan Fire consumed 65% Pinyon-Utah juniper

120 forest and 29% Turbinella oak-alderleaf mountain mahogany shrubland, where 80% of the total carbon emitted came from flaming conditions. On this same day, the ER-2 aircraft flew over the fire in such a way to create a sweeping bowtie pattern, where the fire plume was captured on the downwind side of the bowtie and the background air was captured on the upwind side of the bowtie. This same fire was also sampled by the NASA DC-8 aircraft, equipped with several remote sensing and *in situ* observations of composition, near in time to the ER-2. The DC-8 flew above the Sheridan Fire smoke plume starting

125 at approximately 24 UTC, or 17:00 local time, two hours after the ER-2 started to make measurements. This fire provides an ideal test case to compare plume composition determinations and constrain chemical models of plume evolution.

To approximate the winds driving the Sheridan Fire's smoke plume transport, we use reanalysis data, described in section 2.2. To estimate the height of the winds that we need to sample from the reanalysis data, we need to know the altitude of the

130  smoke plume. The NASA Langley Research Center Differential Absorption Lidar-High Spectral Resolution Lidar (DIAL-HSRL) instrument on the DC-8 aircraft measured vertical profiles of aerosol backscatter at 532 nm, and we approximated the plume altitude to be the most concentrated part of the plume. Altitude was converted to a pressure level by recording the DC-8 aircraft data at a time when the DC-8 was flying through the smoke plume, which resulted in a pressure level of 588 mb.

### 2.2 ERA5

To estimate the wind speeds of the Sheridan Fire smoke plume, we obtained hourly reanalysis data from ECMWF Reanalysis v5 (ERA5), which has a horizontal resolution of 0.25 deg x 0.25 deg (C3S, 2018; Hersbach et al., 2023). We collected zonal and meridional wind speeds at pressures every 25 mb from 1000 mb to 750 mb and every 50 mb from 750 mb to 400 mb. With the smoke plume altitude information from the DIAL-HSRL, the wind speeds over the Sheridan Fire

140  center were determined by interpolating the ERA5 zonal and meridional wind to the time that the ER-2 flew over the fire center, to the longitude and latitude of the fire center, and to the pressure level of the fire plume.

### 2.3 GOES FRP

The Geostationary Operational Environmental Satellites-16 (GOES-16) (East) and GOES-17 (West) provide full-disk snapshots of Earth every five minutes. On both satellites, the Advanced Baseline Imager (ABI) uses visible and infrared

145  spectral bands to locate fires and provide fire characteristics. FRP information was retrieved from both GOES-16 and GOES-17 using the WildFire Automated Biomass Burning Algorithm from the University of Wisconsin, Madison (Schmidt, 2020). A diurnal profile of the Sheridan Fire's sum-FRP, a sum of all fire pixel FRPs associated with the Sheridan Fire, was generated by selecting GOES data within 4 km of the final fire perimeter from the Geospatial Multi-Agency Coordination (GeoMAC). A pseudo-diurnal FRP product was created to represent a more realistic diurnal fire cycle by reallocating 5% of

150  the total daily FRP to the quiescent FRP periods where there are no FRP observations. We smoothed the transition between the quiescent and active FRP periods.

### 2.4 Emission inventories

The derived emission rates from this work are compared to a set of commonly used biomass burning emission inventories, including GFED4s, FINNv2.5, QFEDv2.5, and GFASv1.2 (Darmenov and da Silva, 2015; Giglio et al., 2013; Kaiser et al.,

155  2012; van der Werf et al., 2017; Wiedinmyer et al., 2023). GFED4s is burned area emissions inventory that includes small fires. Monthly emission estimates are calculated by combining burned area maps from 500-m Moderate Resolution Imaging Spectroradiometer (MODIS) data with the Carnegie-Ames-Stanford Approach model, which estimates fuel loads and combustion completeness. Daily emissions estimates stemmed from MODIS data. Conversion to emission rates is achieved by multiplying emission factors to the computed dry matter emissions (Akagi et al., 2011). The spatial resolution is $0.25° \times$

160  $0.25°$ and provides emission data for $NO_x$ as NO, but not $NO_2$ or HONO.

FINNv2.5 is another burned area emissions inventory. It uses the 375-m Visible Infrared Imaging Radiometer Suite (VIIRS) and MODIS at 1 km$^2$ resolution to report active fire detections from which burned area is derived. Emissions are calculated from the following equation, Eq. (1):

$$E_i = A \times B \times FB \times EF_i, \tag{1}$$

where $i$ is a specific compound, $E$ is the emissions, $A$ is the area burned, $B$ is the amount of biomass, $FB$ is the fraction of biomass burned, and $EF$ is the emission factor with units of mass of $i$ per mass biomass burned. The emission factors used in FINNv2.5 are based on updates in the published literature (Akagi et al., 2011; Fang et al., 2017; Liu et al., 2016, 2017; Paton-Walsh et al., 2014; Santiago-De La Rosa et al., 2018; Stockwell et al., 2015; Urbanski, 2014). $NO_2$ is a standard emission product in FINNv2.5. Total non-methane organic gases (NMOG) in FINNv2.5 can also be mapped to species found in three commonly used chemical mechanisms: Statewide Air Pollution Research Center Mechanism (SAPRC99), Model for Ozone and Related chemical Tracers (MOZART), and Goddard Earth Observing System with Chemistry (GOES-Chem). NMOG can be mapped to HONO for use in SAPRC and MOZART; there is no map to HONO for GOES-Chem. The spatial resolution of this inventory is 0.1° × 0.1° and the temporal resolution is daily.

QFEDv2.5 is an FRP-derived emissions inventory. FRP is attained from the MODIS Level 2 products, MODIS/Terra Thermal Anomalies/Fire (MOD14) and MODIS/Aqua Thermal Anomalies/Fire (MYD14). An emissions rate is calculated from the following equation, Eq. (2):

$$E_i = \alpha \times EF_i \times \frac{FRP}{A}, \tag{2}$$

where $E_i$ is the emission rate of compound $i$ per unit area, $\alpha$ is a constant that relates time integrated FRP (fire radiative energy) to dry biomass burned, $EF_i$ is the emission factor of compound $i$, and $A$ is the area of the satellite pixel. The emission factors used in QFEDv2.5 are defined by those in Andreae and Merlet (2001). The spatial resolution is 0.1° × 0.1° and provides daily mean emission data for NO, but not $NO_2$ or HONO.

GFASv1.2 is also an FRP-derived emissions inventory. A dry matter combustion rate is calculated by multiplying land-cover-dependent conversion factors with the FRP areal density. The conversion factor relates FRP to dry matter burned and FRP areal density is total FRP in a grid cell divided by total observed area in a grid cell. Compound emission rates are found by multiplying an emission factor by the dry matter combustion rate. Emission factors are defined by those in Andreae and Merlet (2001). The spatial resolution is 0.1° × 0.1° and provides daily mean emission data for $NO_x$ as NO, but not $NO_2$ or HONO.

### 2.5 Analysis methods

#### 2.5.1 Calculation of HONO and NO₂ line densities

We transformed the ER-2 GCAS HONO and $NO_2$ VCD data into line densities by the following procedure. First, we regridded each GCAS swath within each flight track onto grids with a resolution of 0.0045 degrees (0.5 km), the resolution

195    of the instrument, and interpolated across portions of the grid with missing data. We then subtracted from the entire scene the average HONO and $NO_2$ VCDs upwind of the fire. Subsequently, we rotated the grids by the angle of the time averaged $NO_2$ VCD plume, representing the mean wind direction (Fig. A1). Finally, we summed along the plume in the crosswind direction to produce line densities. This process is visually summarized in Fig. 1.
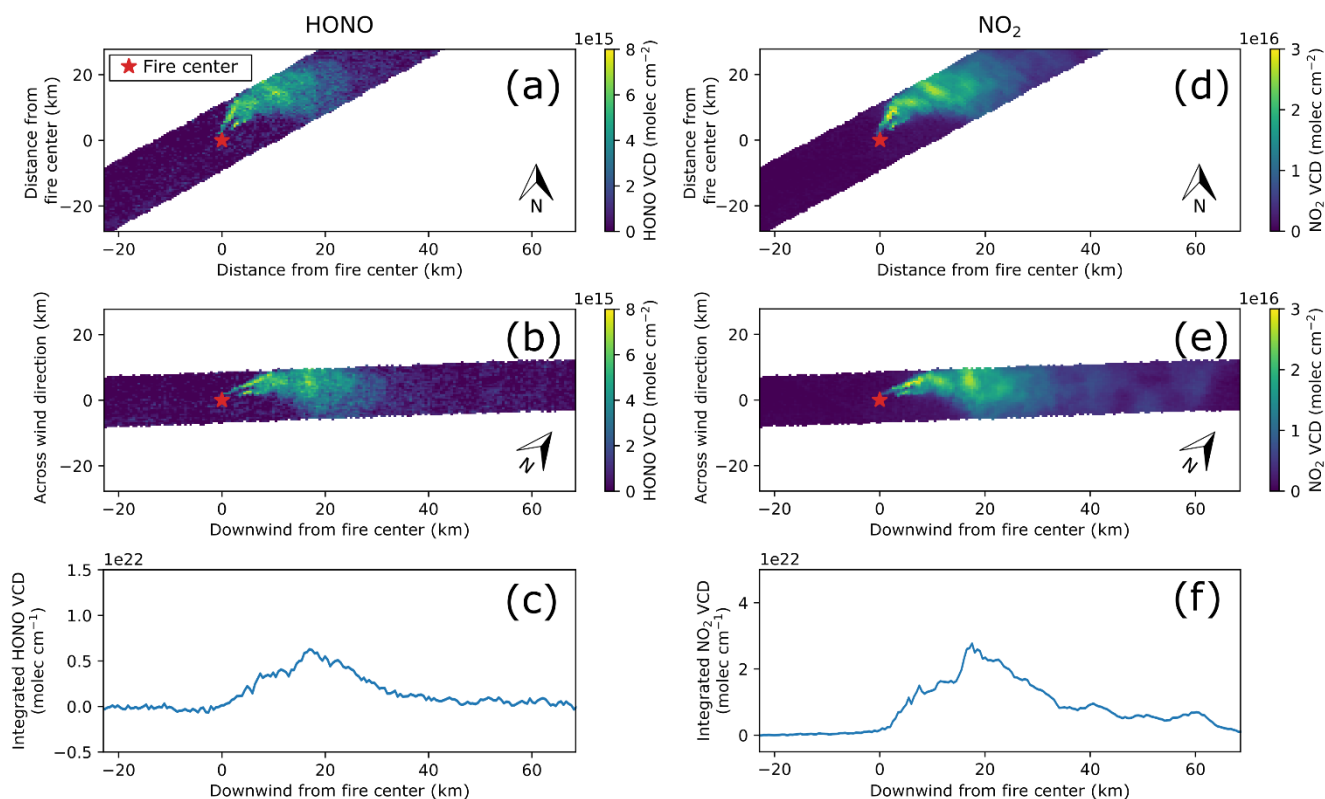


**Figure 1: Image of (a) gridded and (b) rotated track 14 GCAS HONO VCD. (c) HONO line density from track 14. Image of (d) gridded and (e) rotated track 14 GCAS NO₂ VCD. (f) NO₂ line density from track 14.**

Due to the sweeping bowtie flight pattern, only flight tracks 12, 14, and 18 capture the smoke plume core by sampling nearly
205    parallel to the wind direction. Other tracks capture the smoke plume at an angle, thus line densities at these times will be

Atmospheric
Measurement
Techniques
Discussions
Open Access
EGU

incomplete and asymmetric. For the rest of this manuscript, emissions rates and lifetimes will be calculated solely for tracks 12, 14, and 18.

### 2.5.2 Exponentially Modified Gaussian (EMG)

210 In addition to extrapolating from burned area or FRP observations, emissions from biomass burning can also be estimated by directly analyzing the smoke plume chemical concentrations and shape. One such approach relies on fitting an exponentially-modified Gaussian (EMG) to the line density of, for example, daily satellite observations of $NO_2$ columns from the TROPOspheric Monitoring Instrument (TROPOMI) (Jin et al., 2021). The EMG probability density function is the result of a convolution of the exponential and normal probability density functions. EMGs have been applied to satellite observations of OMI and TROPOMI $NO_2$ to estimate emissions and lifetimes from point sources and urban areas (Beirle et

215 al., 2011; De Foy et al., 2015; Goldberg et al., 2019; Laughner and Cohen, 2019; Lu et al., 2015; Xue et al., 2022). Two-dimensional EMGs have been used to estimate $SO_2$ and $NH_3$ emissions and lifetimes (Dammers et al., 2019; Fioletov et al., 2015; McLinden et al., 2020). In addition to satellite data, EMGs were used to estimate emissions of $NO_x$ and $NO_2$ from wildfires with data from field campaigns (Griffin et al., 2021).

220 The EMG function we use in this study is modeled after Jin et al. 2021 and is defined in Eq. (3):

$$L(x|a, x_0, \mu_x, \sigma_x, B) = \frac{a}{2x_0} \exp\left(\frac{\mu_x}{x_0} + \frac{\sigma_x{}^2}{2x_0{}^2} - \frac{x}{x_0}\right) \mathrm{erfc}\left(-\frac{1}{\sqrt{2}}\left(\frac{x - \mu_x}{\sigma_x} - \frac{\sigma_x}{x_0}\right)\right) + B, \quad (3)$$

where $a$ is a scale factor representing the total number of molecules in a plume, $x_0$ is the $e$-folding distance representing the length scale of the exponential decay in km, $\mu_x$ is the location of the apparent source relative to the source center in km and is the center of the Gaussian component, $\sigma_x$ is the square root of the variance of the Gaussian component in km, $B$ is the

225 background in molec km$^{-1}$, and erfc is the complementary error function (Jin et al., 2021). Best guesses for initial values were made following Laughner and Cohen (2019) but in the event that a fitting failed, parameters were manually nudged until the fitting function settled on a solution that mimicked the sample data (Laughner and Cohen, 2019).

From the EMG parameters, an emission rate ($E_{EMG}$) and effective lifetime ($\tau_{EMG}$) can be estimated with Eqs. (4) and (5):

230
$$\tau_{EMG} = \frac{x_0}{w}, \quad (4)$$

$$E_{EMG} = \frac{a}{\tau_{EMG}}, \quad (5)$$

where $w$ is the wind speed. The effective lifetime closely represents a chemical lifetime if the emissions, wind speed and direction are constant, and no deposition occurs (De Foy et al., 2014). The wind speeds used in our EMG fits are the same as described in section 2.2. We will show how the wildly varying temporal behavior of wildfires challenges the basic

235 application of this method.

### 2.5.3 PECANS model

The Python Editable Chemical Atmospheric Numeric Solver (PECANS) model is a flexible, idealized atmospheric chemistry multi-box plume model with Gaussian emissions and idealized transport (Joshua-Laughner and Laughner, 2023; Laughner and Cohen, 2019). In version 0.1.1, users specify the dimensionality of the model, choose to include first-order

240    chemistry and emissions, set an initial chemical condition, and set a constant emission rate.

For this research, we ran 1-D PECANS simulations in four configurations that vary the shape of the emission rates with time: constant emissions, step-change emissions, Gaussian emissions, and FRP-profile emissions. In the first configuration, the emissions rate is kept constant for the entire model run time. In the second configuration, the emissions rate has a step-

245    change halfway through the model run time. In the third configuration, the emissions rate is multiplied by the probability density function of a Gaussian with a mean of 5,000 s and standard deviation of 1,000 s. Finally, in the fourth configuration, the emissions rate is prescribed such that for every time step, the rate is multiplied by the fractional FRP. Fractional FRP is calculated by first interpolating the 5-min pseudo-diurnal FRP product to every second, then by normalizing with the daily total FRP. The last three configurations require manual edits to the emissions_setup.py file in the PECANS code, where

250    multiplication factors are applied to the emissions time series. In a limited run of sensitivity tests, we found that the diffusion coefficients in the x and y dimensions did not significantly affect the EMG calculation of emission rate and lifetimes. A more detailed description of the base model parameters is in Table B1.

### 3 Results and discussion

### 3.1 HONO and $NO_2$ plume structure in the Sheridan Fire

255    In multiple flight overpasses, the GCAS on the ER-2 captured the structures of HONO and $NO_2$ plumes evolving over time. In Fig. 2, we show the rotated, gridded GCAS VCDs for HONO and $NO_2$ at three moments in time: ER-2 track 12, track 14, and track 18. In track 12, there are two local maxima of HONO and $NO_2$. The first local maximum is centered about 7.5 km downwind of the Sheridan Fire for both HONO and $NO_2$. The second local maximum is centered around 12.5 km downwind for both compounds. HONO and $NO_2$ plumes share the same plume edges, but the $NO_2$ plume measurement signal persists

260    through 50 km downwind from the fire, while the HONO signal is lost to noise and the plume edge definition vanishes. In track 14, both HONO and $NO_2$ show two parallel plume lines originating from the fire center, as well as another local maximum around 18 km downwind of the fire. Both plumes have lower VCDs than those detected in track 12. Finally, by the time track 18 occurs, the HONO signal is barely present, with the instrument detecting HONO only as far as 20 km downwind of the fire. However, enhanced $NO_2$ remains detectable as far as 60 km away from the fire. Overall, in all three

265    overpasses, HONO and $NO_2$ share local maxima, plume edges, and plume shape.

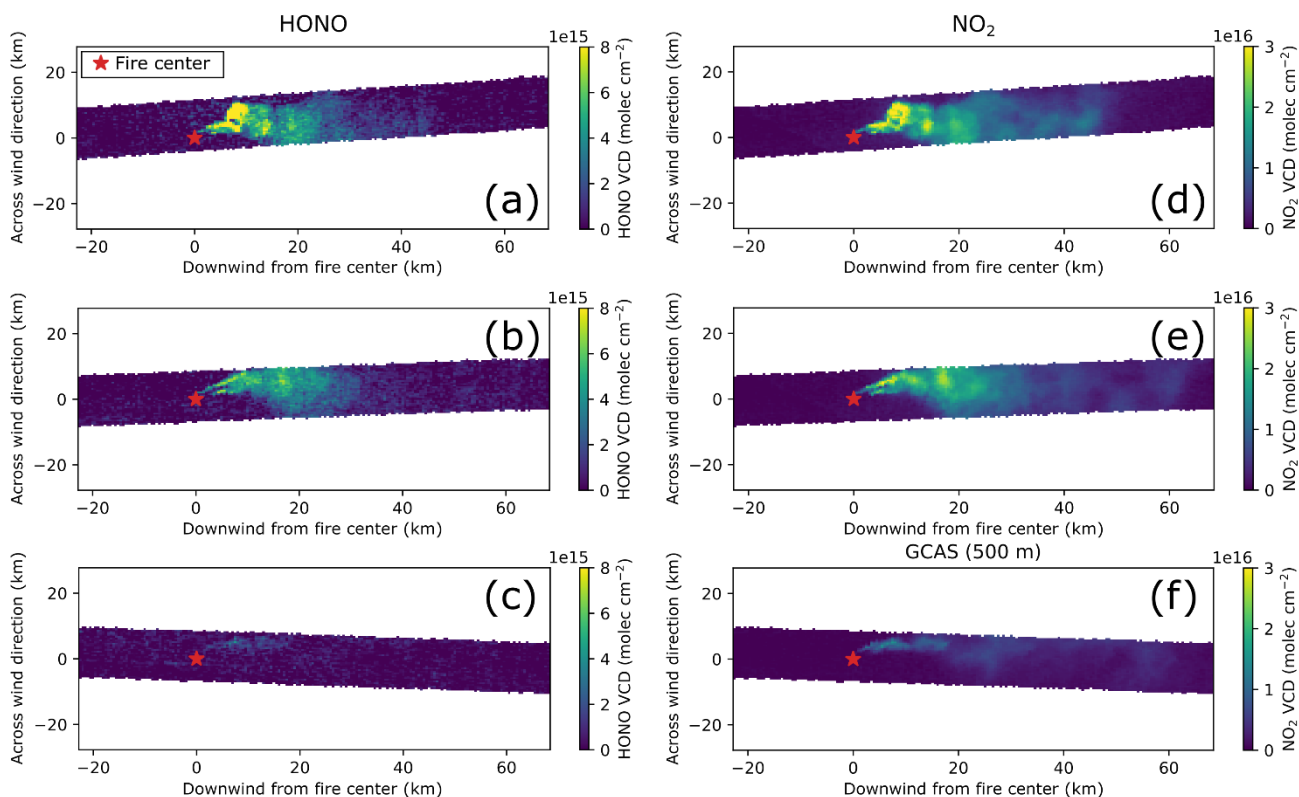Atmospheric
Measurement
Techniques
Discussions



**Figure 2: Images of rotated GCAS HONO VCD for tracks (a) 12, (b) 14, and (c) 18. Images of rotated GCAS NO₂ VCD for tracks (d) 12, (e) 14, and (f) 18.**

270

### 3.2 EMG emission rates and lifetimes from the Sheridan Fire

Emissions from the Sheridan Fire, using sum FRP as a proxy, varied widely over the course of four hours on 16 August 2019 (Fig. 3a). There are features in the GCAS line densities that clearly deviate from an EMG shape. In Fig. 3e, track 12 appears to have a step function decrease in integrated $NO_2$ VCD around 25 km away from the fire center, and another that occurs around 50 km away from the fire center. This change leads to the EMG fit underestimating the line density between 25 and 50 km and overestimating the line density from 50 km to the end. Given that the wind speed is approximately 10 m s$^{-1}$, we infer that the edge of the plume is at 50 km and thus the steep decay is not related to a chemical decay, but a physical edge. HONO appears to have the step function declines in integrated HONO VCD that $NO_2$ demonstrates in track 12 (Fig. 3b), but due to the higher uncertainty in retrievals and its shorter lifetime via photolysis, higher noise in HONO's line density may hide spikes that were present with $NO_2$. This shorter lifetime of HONO may enable use of the standard EMG fit even with time-varying emission rates.
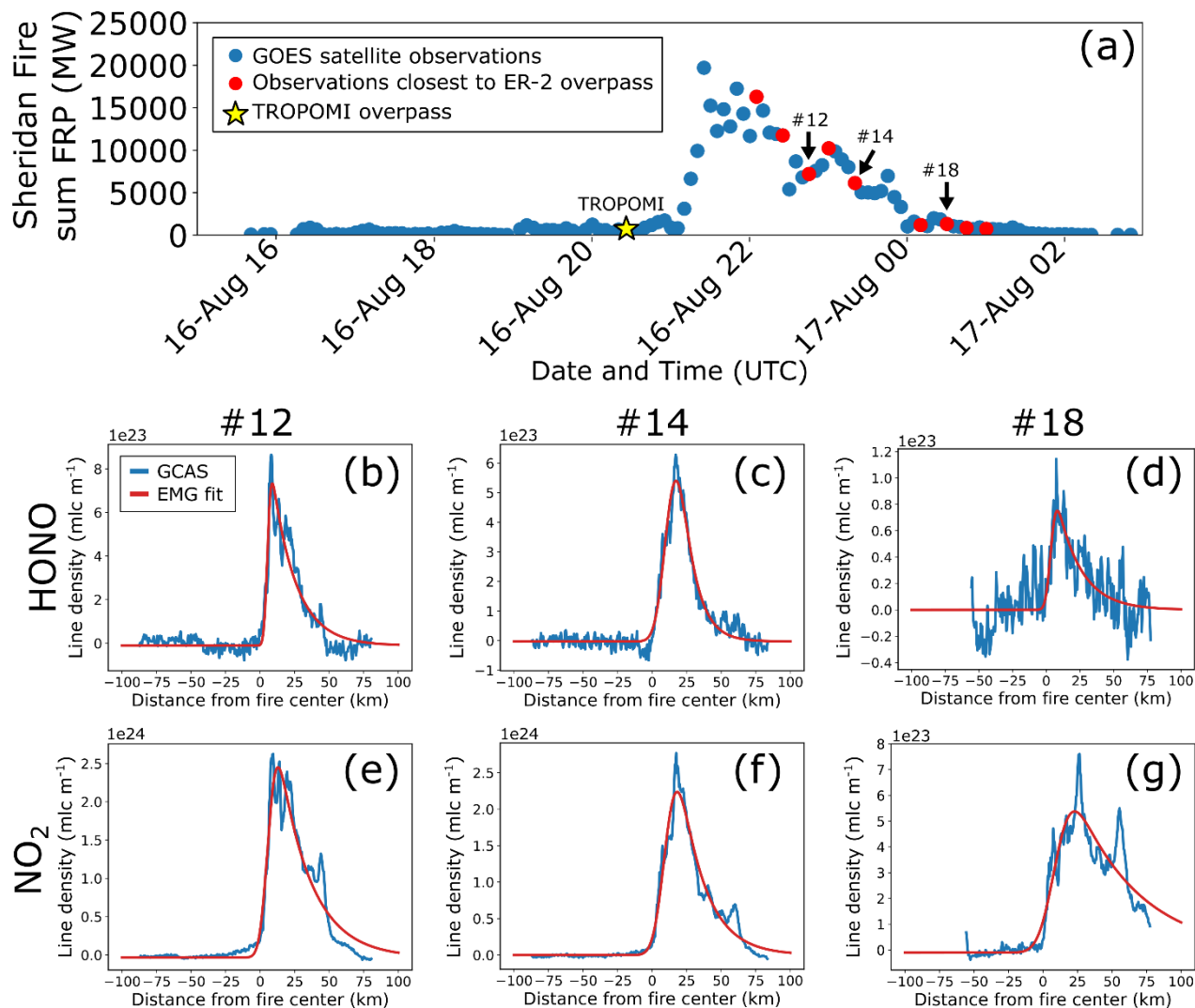
**Figure 3: (a) Sum GOES-16 and GOES-17 FRP in blue with ER-2 overpass times in red. Arrows link ER-2 overpass track**
285 **numbers to the plots below and the TROPOMI overpass time is labeled with a yellow star. (b) Track 12, (c) track 14, and (d) track**
**18 ER-2 GCAS HONO line densities (blue) fit to an EMG (red). (e) Track 12, (f) track 14, and (g) track 18 ER-2 GCAS NO₂ line**
**densities (blue) fit to an EMG (red). Note that y-axis limits are adjusted for each track's maximum HONO and NO₂ value.**

In Figs. 3c and 3f, the track 14 line densities, the EMG fit peaks do not capture the observational maximums, but the EMG

290 fit better captures the observational tails versus their counterparts from track 12 possibly because the smoke plume being

further transported and processed is closer to its inherent steady-state plume shape. In Fig. 3a, we see that by the time the

ER-2 sampled the Sheridan Fire for track 18, sum FRP is nearly at the background value before the Sheridan Fire grew

around 21 UTC. The $NO_2$ line density maximum for track 18 in Fig. 3g is nearly four times smaller than that of track 14 in

11

Atmospheric
Measurement
Techniques
Discussions

Fig. 3f. We assume that the emission rates and lifetimes of HONO and $NO_2$ for track 18 are inaccurate because the EMG fit
295    cannot capture the fact that the fire subsided to near zero power, thus emissions should be zero. This analysis demonstrates
that the EMG functional fit approach for estimating emission rate and lifetime is not always appropriate within a fire's
diurnal cycle: track 12 did not have enough time to reach steady state, track 18 was sampled after the fire died down for the
day, and track 14 was between these extremes. It would not be possible to assess EMG fits in this way applied to single
(once a day) overpasses of a fire.

300

Assuming that HONO and $NO_2$ have similar sampling biases, we can take the ratio of the emissions rates of HONO and $NO_2$
to explore how reactive nitrogen in wildfire smoke is partitioned and processed. In Fig. 4a, the HONO/$NO_2$ emission ratio
decreases with time. A decrease in the emission ratio indicates that over time, less HONO is being emitted than $NO_2$.
Additionally, we find that the HONO/$NO_2$ emission ratio increases with sum FRP (Fig. 4b). This contradicts the foundations
305    of biomass burning emission inventories, which rely on constant emission factors that only vary by land cover type. If this
were true, HONO and $NO_2$ should have a constant emission factor ratio over both time and sum FRP. However, variations in
the emission ratio span a factor of 3 over the course of 2.5 hours. This FRP-dependent behavior of HONO relative to $NO_2$
was reported previously based on satellite-retrieved concentrations closest to Australian wildfires (Fredrickson et al., 2023).
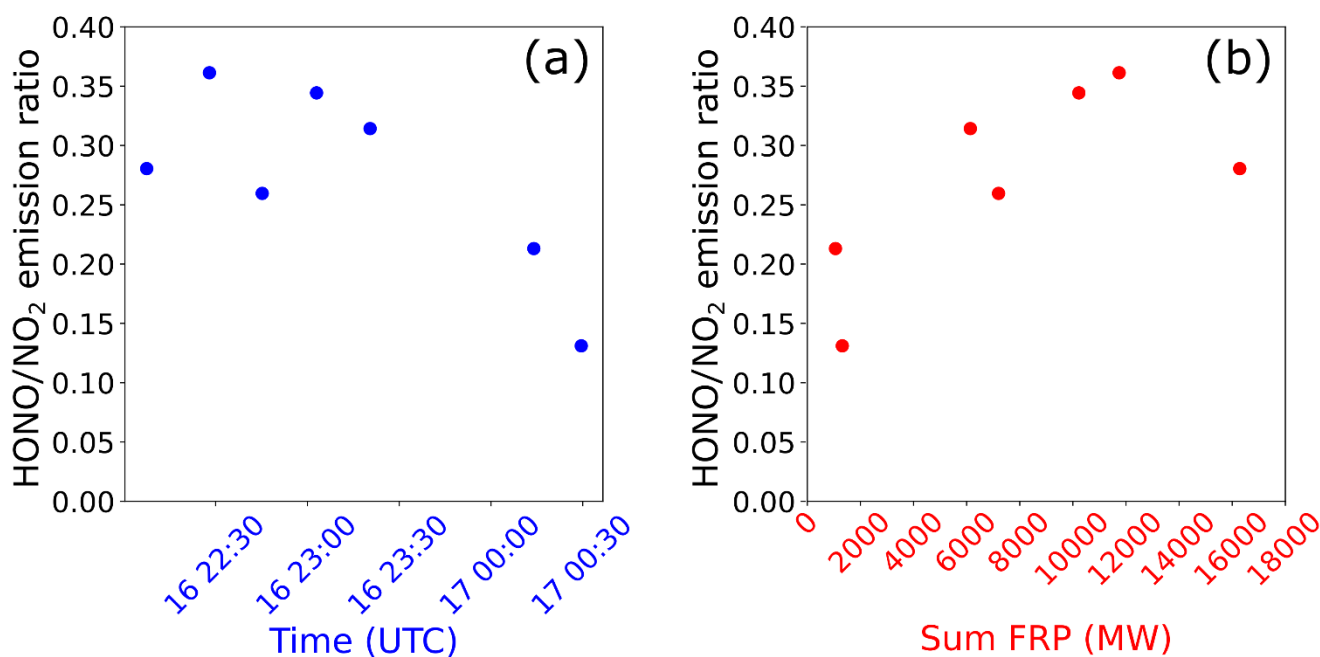


Figure 4: The emission ratio of HONO to $NO_2$ plotted against (a) time and (b) sum FRP for the Sheridan Fire.

310

### 3.3 An improved EMG methodology: Monte Carlo diurnal 1-D models

As alluded to previously, a basic application of the EMG method is rarely suitable for daily observations of wildfires as
315  applied in previous studies (Griffin et al., 2021; Jin et al., 2021). First, a fire may not have had enough time
to have its smoke and emission products transported to provide a complete picture of the decay due to loss processes. The
EMG fit would therefore underestimate the lifetime. We found evidence of this behavior in Fig. 3e.

In Fig. 5, we ran idealized simulations of a hypothetical compound to analyze the accuracy of EMG fits over time. As shown
320  in Fig. 5a, the smoke plume from an idealized 1-D simulation with constant emissions (see Section 2.5.3 and Table B1 for
model configuration) reaches steady state within the model run time. While the model emissions source is centered at 25 km,
the line density peak is shifted to the right due to wind transport. We fit an EMG to the model output every 200 s and
compared the fit results to the model inputs by plotting the ratio of the fit parameter to the model prescribed parameter,
shown in Fig. 5b. At model run times greater than 5000 s, the ratios of EMG fit parameters and model prescribed values for
325  both the emission rate and lifetime approach 1, indicating near equivalence and thus accurate EMG results. However, when
fitting EMGs to plumes modeled at earlier times, the lifetime is underestimated by as much as 97% while the emission rate is
overestimated up to 550%.

Second, wildfire emissions and intensity change over time on an hourly or shorter timescale, while the EMG profile shape
330  assumes that the emission rate has been constant. In Fig. 5c, the emission rate used in the model is halved halfway through
the simulation, i.e., the step-change emissions simulation. The steady-state maximum in the line density near 25 km starts to
decrease after emissions are halved and a secondary peak in line density is observed traveling to the right as the initial high-
emission plume decays. After the emissions are halved, comparison with the EMG fit/model prescribed ratios show that the
emission rate is at first overestimated, then slightly underestimated (Fig. 5d). On the other hand, the lifetime is at first
335  unaffected by the change in emission rate, but then becomes overestimated as the peak from the high-emission times is
transported downwind and lengthens the line density shape.

In Fig. 5e, we applied the EMG method to an idealized simulation with temporally varying emissions that followed a
Gaussian, which is a better approximation of fire behavior than the previous simulations. The Gaussian emission profile used
340  as input to the PECANS model is shown in Fig. B1. Instead of the presence of two line density peaks as in Fig. 5c, only one
line density peak persists through the model simulation (Fig. 5e). By the end of the model run, the line density peak has
shifted from roughly 25 km to 70 km downwind. As shown in Fig. 5f, the EMG determined emission rate initially
overestimates the model prescribed value, but then approaches the true value from 1000 to 2500 s. As the emission rate
grows (Fig. B1) with time, the EMG determined emission rate separates from the model prescribed value, overestimating
345  once more, and eventually grows towards infinity (Fig. 5f). This behavior occurs because the Gaussian emission profile

Atmospheric
Measurement
Techniques
Open Access
EGU
Discussions

approaches zero near the end of the model run, while the plume persists. The EMG determined lifetime, on the other hand, is consistently underestimated. This behavior occurs because not enough time has passed for the inherent line density shape to be realized before the modeled emission rate starts to decline after reaching peak emissions. This decrease in emission rate leads to the shifting of the line density peak downwind, shortening the e-folding distance used to calculate the lifetime. Thus,

350    shifts in emissions will lead to shifts in lifetime, making this Gaussian simulation even more complicated for the EMG method to fit.

Third, wildfires have been observed to increase their thermal output after the 1:30 PM local time that TROPOMI and some other polar-orbiting satellites observe at, and thus daily estimates from the EMG method may underestimate maximum

355    emission rate. We see that for the Sheridan Fire, TROPOMI missed the fire altogether, as TROPOMI made its overpass around 20:25 UTC (Fig. 3a).
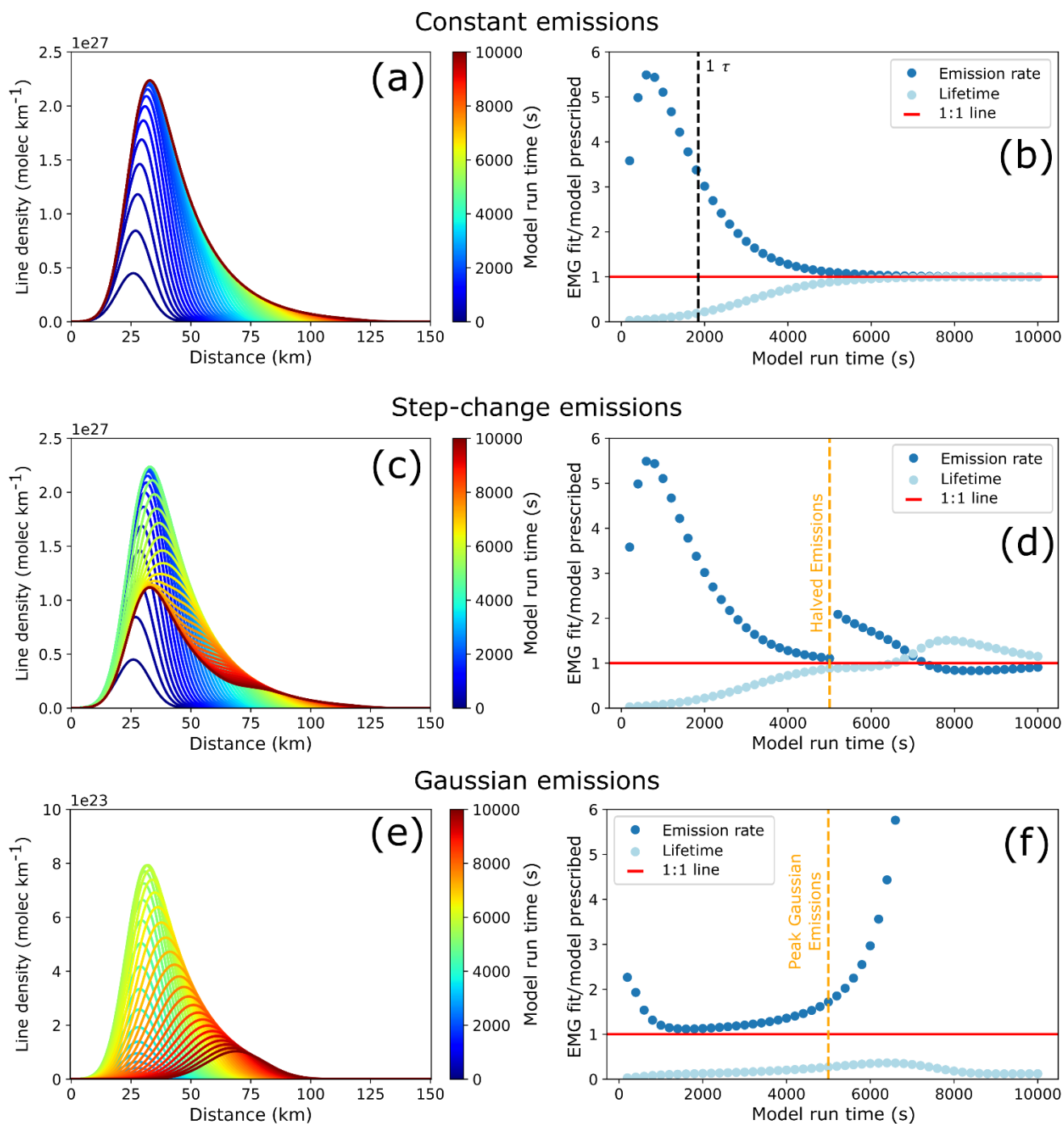
Figure 5: (a) Line densities of a hypothetical compound from a 1-D model with prescribed chemical lifetime of 30.8 minutes and
360   constant emissions colored by model run time. (b) EMG fit / model prescribed emission rate (blue) and lifetime (light blue) at
every model output step through the course of the entire model runtime. The model time equal to the model lifetime is indicated
with a vertical, black dashed line. (c) Line densities for a 1-D model where the emission rate is halved halfway through the model
runtime, colored by model run time. (d) Similar to (b), but for the model in (c). The vertical, gold dashed line indicates where the

15

365 emissions were halved. (e) Line densities for a 1-D model where the emissions are scaled to a Gaussian PDF with a mean of 5000 and standard deviation of 1000, colored by model run time. (f) Similar to (b), but for the model in (e). The vertical, gold dashed line indicates peak Gaussian emissions.

The above results illustrate that the application of EMGs to wildfire plumes should improve with hourly observations of wildfire pollutants as will become possible with the TEMPO instrument or another geostationary satellite instrument that

370 measures atmospheric composition. As emission rates are initially overestimated from the EMG approach early in the fire growth, using observations that are at least forty minutes later than fire start (past some FRP threshold; see Fig. C1), and analogously discarding observations after the fire intensity has diminished will both increase accuracy of the EMG estimates of emissions and lifetime.

375 The EMG method is inherently limited in that the emissions and lifetime are coupled due to an underdetermined system. We address this issue by improving constraints on the time-varying emissions using observed FRP variations together with a Monte Carlo application of the 1-D model to sample a large parameter space of lifetime and emission conditions. The diurnal FRP shape is obtained by dividing the summed GOES-16 and GOES-17 5-minute FRP product by the GOES total daily FRP. EMG functions are fit to all appropriate satellite observations (see above) and the ranges of EMG fit lifetimes and total

380 emission rate divided by the fractional FRP are used to create sampling distributions for a Monte Carlo simulation. We run the 1-D PECAN model one hundred times, varying the lifetime and total emission rate parameters based on the distributions. The coefficient of determination, $R^2$, between the model and the satellite observations is shown in Fig. 6 for HONO and $NO_2$. The absolute maximum $R^2$ provides an indication of the most likely lifetime and emissions rate combination(s).

385 In Fig. 6, the emission rate has an inverse relationship with lifetime, which is expected since general mass balance constitutes that concentration is proportional to emissions and inversely proportional to loss rate. In Figs. 6a and 6b, the largest $R^2$ (above 0.9) between the HONO observed and model derived line densities occur with a lifetime between 15 and 27 minutes and an emissions rate of 0.6 to $1.35 \times 10^{25}$ molec s$^{-1}$. In Figs. 6c and 6d, $NO_2$ has a larger viable range of lifetimes and total emissions rates, which range between 15 and 45 minutes and 2.0 to $5.5 \times 10^{25}$ molec s$^{-1}$, respectively.

390 Track 18 was excluded from this analysis as measurements occurred after the Sheridan Fire had ceased its high emissions for the day. The model runs with the largest $R^2$ values are shown in Fig. D1. In Fig. D1d, the model enables EMG fits to non-EMG shapes in the observed multi-model line density, which is not possible with the basic application of the EMG method (Fig. 3f).

16

Atmospheric
Measurement
Techniques
Discussions
Open Access
EGU
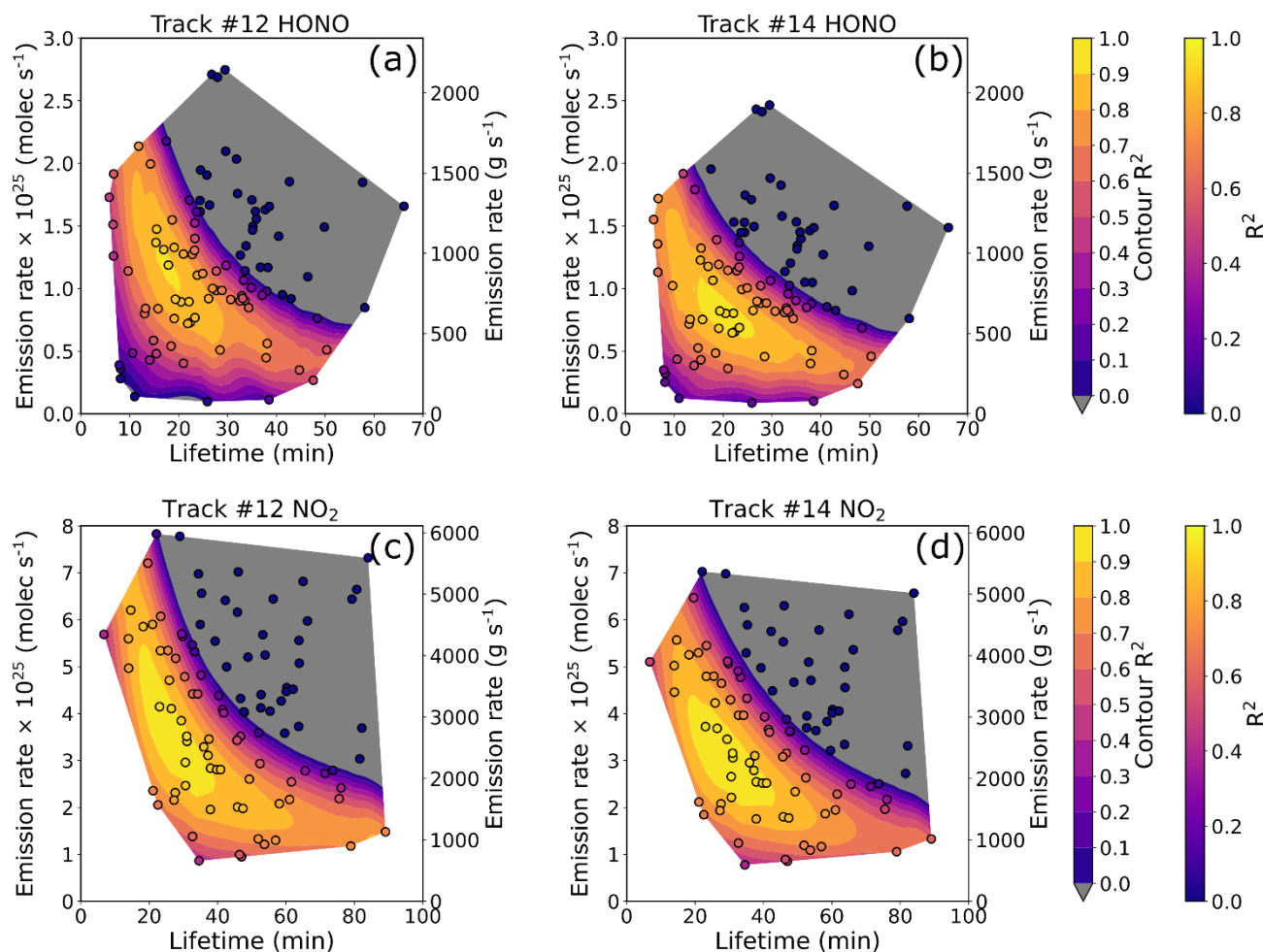
**Figure 6: The $R^2$ value between 100 PECANS models with varied total emission rate and lifetime model input parameters and the observed GCAS HONO VCD line density for (a) track 12 and (b) track 14. A filled contour map creates a 2D interpolation of the randomly sampled models (circles). (c) and (d) Similar to (a) and (b), but for GCAS NO₂ VCD.**

The lifetime of HONO from photolysis alone just above the smoke plume, estimated from the TUV Quick Calculator (https://www.acom.ucar.edu/Models/TUV/Interactive_TUV/), would be 13 min and 15 min during the overpasses of track 12 and 14 respectively, which is shorter than those lifetimes found in Figs. 6a and 6b. Likely, HONO is photolyzing on the plume edges, but HONO deeper in the plume from which the retrieval is obtained likely has longer lifetimes as proposed in earlier literature (Wang et al., 2021). The NO₂ lifetime for the Sheridan Fire we find from the Monte Carlo approach is smaller than most cited in the literature and still smaller than those values used in model assumptions. In multiple satellite $NO_x$ observational studies, a $NO_x$ lifetime of 2 hours is typically assumed to infer mass emission rates and emission coefficients of $NO_x$ from wildfires, citing previous field and model studies (Mebust et al., 2011; Mebust and Cohen, 2014).

Other studies use a $NO_x$ lifetime of 6 hours for fires, citing lifetimes of $NO_x$ found using satellite observations over megacities, as well as from an aircraft campaign sampling biomass burning plumes in northern Australia (Schreier et al., 2014, 2015; Tanimoto et al., 2015). Other studies report $NO_x$ lifetimes within or above this range (Akagi et al., 2012; Berezin et al., 2016; Takegawa et al., 2003). Only two studies reported $NO_x$ lifetimes under 2 hours in wildfire plumes sampled with aircraft in the western US (Juncosa Calahorrano et al., 2021b; Wolfe et al., 2022). One other satellite study used OMI $NO_2$ satellite retrievals from the 2016 Horse River wildfire in Alberta Canada and reported a range of $NO_2$ lifetimes from 1 to 2.5 hours (Adams et al., 2019). Two other studies used EMG and flux methods to estimate the lifetime of $NO_x$ from wildfires. Jin et al. (2021) reported a range of $NO_x$ lifetimes from 0.8 to 10.5 hours using the EMG method and Griffin et al. (2021) reported three different ranges based on the method (Griffin et al., 2021; Jin et al., 2021). Using EMG on TROPOMI observations, the $NO_x$ lifetime ranged from 1 to 3 hours, while EMG applied to field campaign data ranged from 0.9 to 6.5 hours and using EMG on model VCDs ranged from 0.5 to 1.5 hours (Griffin et al., 2021).

It is beyond the scope of this paper to provide an in-depth exploration of the source of our shortened $NO_2$ lifetime, especially given the single fire we examine here. It is worth repeating that the EMG method derives an effective lifetime, not a chemical lifetime. The effective lifetime also includes influences from plume meandering, deposition, sampling issues, and other factors, meaning that effective lifetimes are usually shorter than chemical lifetimes (De Foy et al., 2014; Lu et al., 2015). However, a simple chemical box model applied to the Sheridan Fire indicates that a large source of organic peroxy radicals ($RO_2$) is needed to drive the $NO_2$ chemical lifetime to the short values we infer from applying the 1-D plume model (with no chemical mechanism) to the GCAS observations.

### 3.4 Biomass burning emission inventories underestimate observationally constrained emission estimates

We compare our Monte Carlo diurnal 1-D model HONO and $NO_2$ emissions with those reported in other biomass burning emissions inventories. As shown In Fig. 7a, FINNv2.5 HONO emissions for the SAPRC and MOZART mechanisms underestimate the minimum and maximum daily mean emission rate of our method (MC diurnal 1-D) by a factor of 5 for the minimum and a factor of 10 for the maximum. In contrast our Monte Carlo diurnal 1-D model $NO_2$ emissions estimates fall in the middle of the four emissions inventories. Our method exceeds the estimates of bottom-up approaches but is exceeded by the estimates of top-down approaches. QFED has the largest $NO_2$ emissions and is nearly 5 times the GFASv1.2 estimate. For the Sheridan Fire, HONO emissions are underestimated by biomass burning emission inventories, but $NO_2$ emissions are in the range estimated by the other inventories.
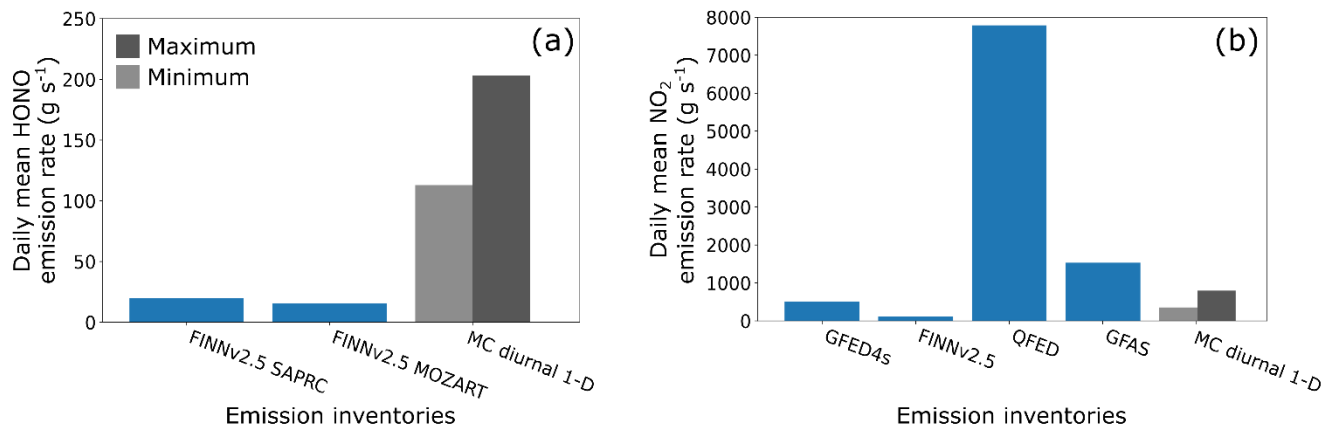
Figure 7: Daily mean emissions of (a) HONO and (b) NO₂ from the Monte Carlo diurnal 1-D model method (MC diurnal 1-D) using the $R^2$ = 0.9 contour to define the minimum and maximum emissions, and the following biomass burning emission inventories: FINNv2.5 SAPRC, FINNv2.5 MOZART, GFED4s, FINNv2.5, QFEDv2.5, and GFASv1.2.

## 4 Conclusions

Using high-resolution remote observations of fire plumes from the GCAS instrument on the NASA ER-2 during the FIREX-AQ campaign, we estimated the evolving emission rates and lifetimes of HONO and $NO_2$ from the Sheridan Fire. We observed the evolving plume structure of HONO and $NO_2$, as well as the HONO/$NO_2$ emission ratio that decreased in time and increased with sum FRP, similar to previous findings with HONO/$NO_2$ concentrations in Australian wildfires (Fredrickson et al., 2023). Using a 1-D horizontal Gaussian emission, first-order chemical model, we found that the EMG method to estimate emissions and lifetimes requires emissions from a fire to be relatively constant over several chemical and transport lifetimes. Idealized simulations of time varying fire emissions, transport and chemical loss illustrated the challenge of applying EMG to single overpass line density observations to derive emissions and lifetime estimates. Using Monte Carlo 1-D horizontal models developed with the diurnal FRP profile of the Sheridan Fire and the continuously sensed plume composition by the GCAS instrument, we provided constraints on the emission rate and lifetime of HONO and $NO_2$. The $NO_2$ lifetime is on the order of 20 to 40 minutes for this fire, which is on the lower end of reported wildfire $NO_2$ and $NO_x$ lifetimes. We hypothesize a large source of $RO_2$ drives the loss of $NO_x$. The HONO lifetime is longer than the expected clear-sky photolysis lifetime and consistent with a large fraction of the measured HONO column being in the core of the smoke plume with lower light levels and thus longer photolysis lifetimes. The HONO emissions using the Monte Carlo 1-D models were 5 to 10 times larger than that from both FINNv2.5 chemical mechanisms. On the other hand, the $NO_2$ emissions were larger than burned-area-based biomass burning emission inventories but were dwarfed by the FRP-based biomass burning emission inventories.

The Monte Carlo diurnal 1-D model procedure may not work well for all fires and has the following limitations. This procedure assumes that there is an individual fire with a constant-direction wind transporting the smoke plume. If there are multiple fires whose smoke plumes coalesce, this improved EMG will fail to estimate the true emission rate and lifetime, due

465  to multiple point sources in different locations contributing their own unique time-varying emissions. These limitations apply to the regular EMG fit approach as well. In addition, trace-gas retrievals from UV-Vis measurements can have significant uncertainties arising from retrieval method and various auxiliary information such as a-priori vertical profile shapes, aerosols, etc. used in retrievals.

470  This study indicates the need for future research into HONO emissions quantification and for the impacts of HONO emissions on the chemistry downwind in a fire plume. We were only able to compare our HONO emissions to one biomass burning emission inventory, FINN v2.5, whereas we could compare $NO_2$ to at least four other inventories. Applying our methodology to hourly daytime observations of fires will improve the representation of HONO emissions from fires and therefore its impacts our understanding of fire plume reactive chemistry. With the launch of Tropospheric Emissions:

475  Monitoring of Pollution (TEMPO) instrument in early April 2023, hourly daytime measurements of air pollutants are possible in the North American continent. Future research promises to narrow the uncertainty of wildfire emissions, emissions that evolve on a sub-hourly basis. The Monte Carlo diurnal 1-D model approach is primed for application on fires detected by TEMPO and the Geostationary Environment Monitoring Spectrometer (GEMS).

**Appendix A: Plume rotation**
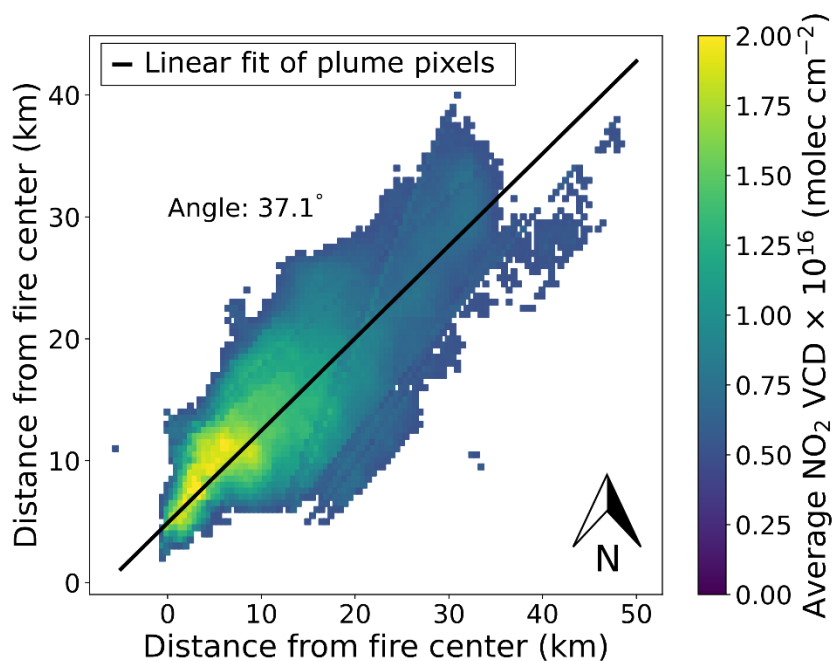


**Figure A1: Time-averaged NO₂ VCD plume, where plume pixels were more than 3 times greater than the NO₂ upwind background. The black line is a linear fit of the plume pixels, where the standard deviation at each location was the difference between the maximum NO₂ VCD and the location's NO₂ VCD. The angle of the line is displayed.**

480

**Appendix B: Idealized model simulation construction**

485    **Table B1: Detailed PECANS 1-D Model Configuration for Idealized Simulations**

| Model Parameter | Model Quantity |
|---|---|
| Model timestep | 1 s |
| Run time | 10,000 s |
| Number of boxes in each dimension | x: 500 |
| | y: 0 |
| | z: 0 |
| Size of boxes in each dimension | x: 500 m |
| | y: 500 m |
| | z: 500 m |
| Transport scheme | Implicit2 |

Atmospheric
Measurement
Techniques
Open Access
Discussions
EGU

| | |
|---|---|
| Wind type | Fixed |
| Wind speeds in each dimension | x: 9.88 m s$^{-1}$ |
| | y: 0 m s$^{-1}$ |
| | z: 0 m s$^{-1}$ |
| Diffusion coefficient in each dimension | x: 100 m$^2$ s$^{-1}$ |
| | y: 0 m$^2$ s$^{-1}$ |
| | z: 0 m$^2$ s$^{-1}$ |
| Chemical mechanism | Ideal first-order |
| Lifetime | 1848 s |
| Initial condition | Gaussian |
| Initial condition options | center_x: 25,000 m |
| | width_x: 3,000 m |
| | height: 0 molec cm$^{-3}$ |
| Emission type | Gaussian |
| Emission options | center_x: 25,000 m |
| | width_x: 6,770 m |
| | total: 4.04e+25 |
| | molec s$^{-1}$ |
| Model output frequency | 200 s |

Atmospheric
Measurement
Techniques
Discussions

Open Access
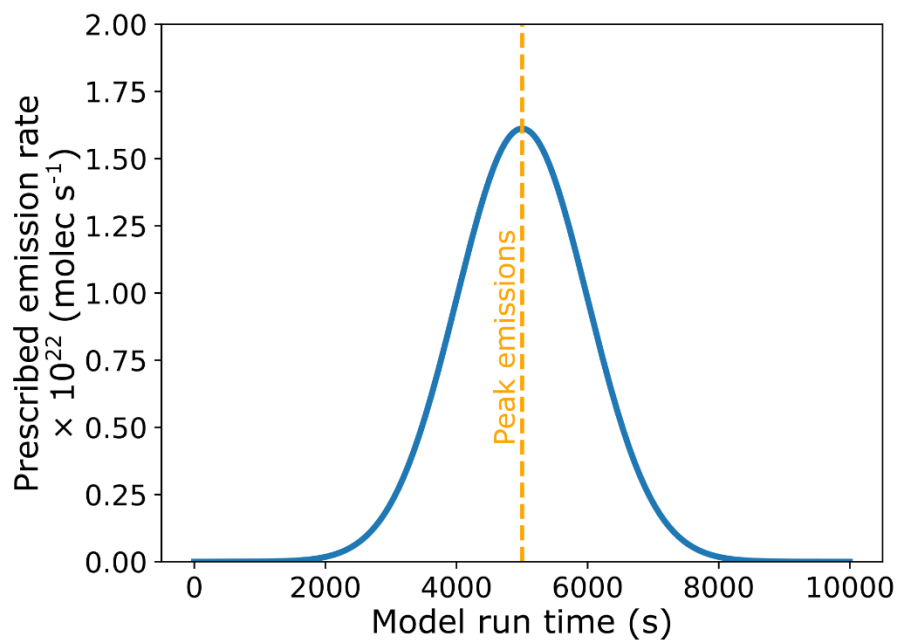


**Figure B1: Gaussian emission rate profile of the PECANS Gaussian emissions model run (Figs. 5e and 5f). Peak emissions occur at 5000 s model runtime indicated by the gold vertical dashed line.**

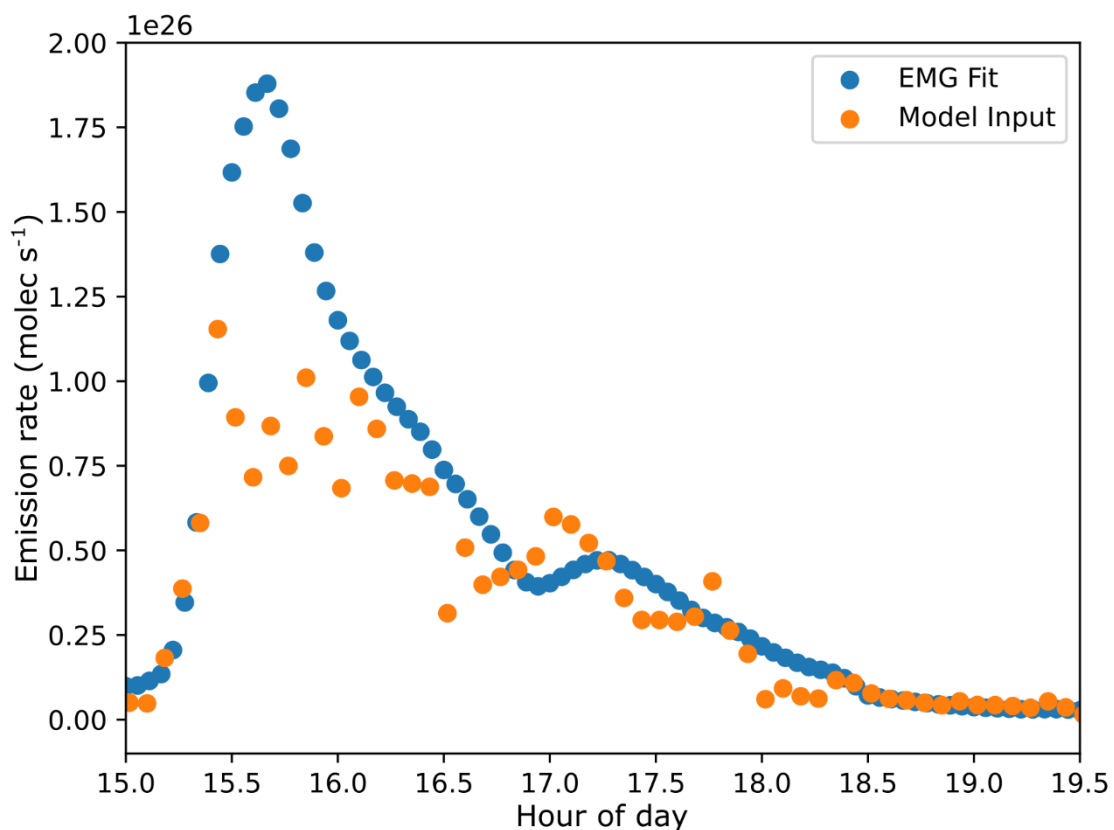# Appendix C: Constraints on the Monte Carlo diurnal 1-D model method



**Figure C1: Model input emission rate (molec s⁻¹) of a diurnal FRP profile source (orange) and the emission rate estimated from the EMG fit method applied to modeled line densities every 200 seconds (blue). The EMG fits overestimate the model input emission rate as the fire grows in output and lasts for approximately 40 minutes.**

Atmospheric
Measurement
Techniques
Discussions

Open Access
EGU

495 **Appendix D: Best fit models from Monte Carlo diurnal 1-D model method**
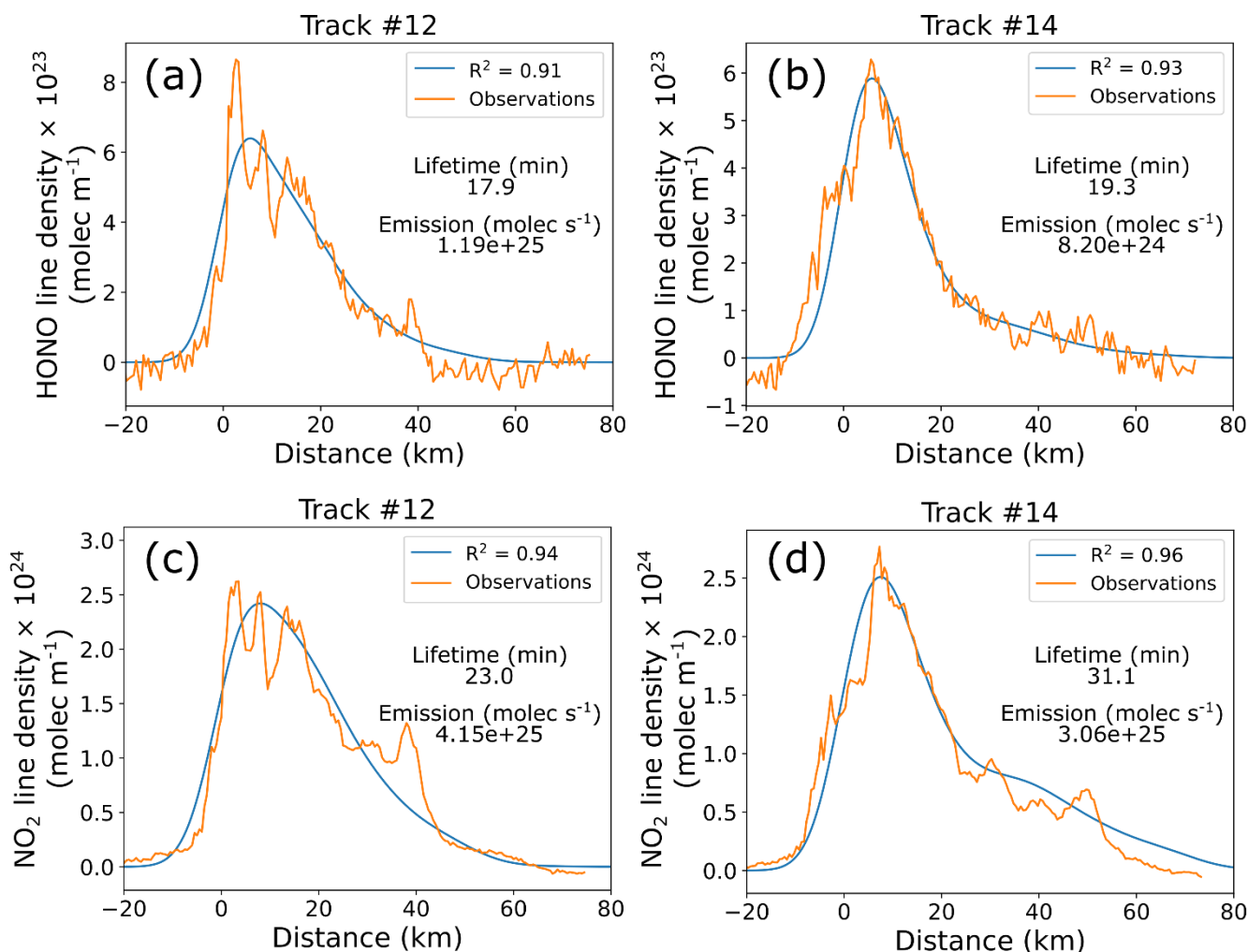


**Figure D1: Observed GCAS VCD line densities (orange) and best Monte Carlo diurnal 1-D model line densities (blue) for (a) HONO track 12, (b) HONO track 14, (c) NO₂ track 12, and (d) NO₂ track 14. Model lifetimes and emission rates are reported in the subfigures.**

500 **Code availability**

The PECANS model is available on GitHub (https://github.com/joshua-laughner/PECANS, last accessed 28 July 2024). This work used a customized version of PECANS v0.1.1; the customized version is available at https://doi.org/10.5281/zenodo.13621859.

Atmospheric
Measurement
Techniques
Discussions

**Data availability**

505   The FIREX-AQ aircraft datasets are available at https://www-air.larc.nasa.gov/cgi-bin/ArcView/firexaq and includes ER-2 GCAS data, the Fuel2Fire ecosystems-burned analysis, the Fuel2Fire GOES FRP diurnal cycle analysis, DC-8 DIAL-HSRL data, DC-8 photolysis data, and DC-8 aircraft data (last access: 8 September 2024) (FIREX-AQ Science Team, 2019). The ERA-5 reanalysis dataset is available at https://cds.climate.copernicus.eu/cdsapp#!/dataset/reanalysis-era5-pressure-levels?tab=overview (last access: 16 September 2024) (Hersbach et al., 2023). The GFED4s emission inventory data is

510   available at https://www.geo.vu.nl/~gwerf/GFED/GFED4/ (last access: 16 September 2024) (van der Werf et al., 2017). The FINNv2.5 emission inventory data is available at https://rda.ucar.edu/datasets/d312009/ (last access: 16 September 2024) (Wiedinmyer and Emmons, 2022). The QFEDv2.5 emission inventory data is available at https://portal.nccs.nasa.gov/datashare/iesa/aerosol/emissions/QFED/v2.5r1/0.25/QFED/ (last access: 16 September 2024) (Darmenov and da Silva, 2015). The GFASv1.2 emission inventory data is available at

515   https://ads.atmosphere.copernicus.eu/cdsapp#!/dataset/cams-global-fire-emissions-gfas?tab=overview (last access: 16 September 2024) (Kaiser et al., 2012).

**Author contribution**

CDF and JAT conceived of the project. CDF conducted the analysis and paper drafting. SJJ and LNL provided data and input on results. UAJ processed and provided GFED4s fire emission data. JLL provided PECANS model code and input on

520   results. All authors contributed to manuscript review and editing.

**Competing interests**

At least one of the co-authors is a member of the editorial board of Atmospheric Measurement Techniques.

## References

Adams, C., McLinden, C. A., Shephard, M. W., Dickson, N., Dammers, E., Chen, J., Makar, P., Cady-Pereira, K. E., Tam, N., Kharol, S. K., Lamsal, L. N., and Krotkov, N. A.: Satellite-derived emissions of carbon monoxide, ammonia, and nitrogen dioxide from the 2016 Horse River wildfire in the Fort McMurray area, Atmos. Chem. Phys., 19, 2577–2599, https://doi.org/10.5194/acp-19-2577-2019, 2019.

Akagi, S. K., Yokelson, R. J., Wiedinmyer, C., Alvarado, M. J., Reid, J. S., Karl, T., Crounse, J. D., and Wennberg, P. O.: Emission factors for open and domestic biomass burning for use in atmospheric models, Atmos. Chem. Phys., 11, 4039–4072, https://doi.org/10.5194/acp-11-4039-2011, 2011.

Akagi, S. K., Craven, J. S., Taylor, J. W., McMeeking, G. R., Yokelson, R. J., Burling, I. R., Urbanski, S. P., Wold, C. E., Seinfeld, J. H., Coe, H., Alvarado, M. J., and Weise, D. R.: Evolution of trace gases and particles emitted by a chaparral fire in California, Atmos. Chem. Phys., 12, 1397–1421, https://doi.org/10.5194/acp-12-1397-2012, 2012.

Andreae, M. O.: Emission of trace gases and aerosols from biomass burning – an updated assessment, Atmos. Chem. Phys., 19, 8523–8546, https://doi.org/10.5194/acp-19-8523-2019, 2019.

Andreae, M. O. and Merlet, P.: Emission of trace gases and aerosols from biomass burning, Global Biogeochem. Cycles, 15, 955–966, https://doi.org/10.1029/2000GB001382, 2001.

Beirle, S., Boersma, K. F., Platt, U., Lawrence, M. G., and Wagner, T.: Megacity Emissions and Lifetimes of Nitrogen Oxides Probed from Space, Science, 333, 1737–1739, https://doi.org/10.1126/science.1207824, 2011.

Berezin, E., Konovalov, I., and Romanova, Y.: Inverse Modeling of Nitrogen Oxides Emissions from the 2010 Russian Wildfires by Using Satellite Measurements of Nitrogen Dioxide, in: Proceedings of The 1st International Electronic Conference on Atmospheric Sciences, The 1st International Electronic Conference on Atmospheric Sciences, Sciforum.net, B003, https://doi.org/10.3390/ecas2016-B003, 2016.

Bernath, P., Boone, C., and Crouse, J.: Wildfire smoke destroys stratospheric ozone, Science, 375, 1292–1295, https://doi.org/10.1126/science.abm5611, 2022.

Buysse, C. E., Kaulfus, A., Nair, U., and Jaffe, D. A.: Relationships between Particulate Matter, Ozone, and Nitrogen Oxides during Urban Smoke Events in the Western US, Environ. Sci. Technol., 53, 12519–12528, https://doi.org/10.1021/acs.est.9b05241, 2019.

C3S: ERA5 hourly data on single levels from 1940 to present, https://doi.org/10.24381/CDS.ADBB2D47, 2018.

Dammers, E., McLinden, C. A., Griffin, D., Shephard, M. W., Van Der Graaf, S., Lutsch, E., Schaap, M., Gainairu-Matz, Y., Fioletov, V., Van Damme, M., Whitburn, S., Clarisse, L., Cady-Pereira, K., Clerbaux, C., Coheur, P. F., and Erisman, J. W.: NH3 emissions from large point sources derived from CrIS and IASI satellite observations, Atmos. Chem. Phys., 19, 12261–12293, https://doi.org/10.5194/acp-19-12261-2019, 2019.

Darmenov, A. and da Silva, A.: The Quick Fire Emissions Dataset (QFED): Documentation of versions 2.1, 2.2 and 2.4, NASA Goddard Space Flight Center, Greenbelt, MD, 2015.

Atmospheric
Measurement
Techniques
Discussions

De Foy, B., Wilkins, J. L., Lu, Z., Streets, D. G., and Duncan, B. N.: Model evaluation of methods for estimating surface emissions and chemical lifetimes from satellite data, Atmospheric Environment, 98, 66–77, https://doi.org/10.1016/j.atmosenv.2014.08.051, 2014.

570 De Foy, B., Lu, Z., Streets, D. G., Lamsal, L. N., and Duncan, B. N.: Estimates of power plant NOx emissions and lifetimes from OMI NO2 satellite retrievals, Atmospheric Environment, 116, 1–11, https://doi.org/10.1016/j.atmosenv.2015.05.056, 2015.

Decker, Z. C. J., Wang, S., Bourgeois, I., Campuzano Jost, P., Coggon, M. M., DiGangi, J. P., Diskin, G. S., Flocke, F. M., Franchin, A., Fredrickson, C. D., Gkatzelis, G. I., Hall, S. R., Halliday, H., Hayden, K., Holmes, C. D., Huey, L. G., Jimenez, J. L., Lee, Y. R., Lindaas, J., Middlebrook, A. M., Montzka, D. D., Neuman, J. A., Nowak, J. B., Pagonis, D., 575 Palm, B. B., Peischl, J., Piel, F., Rickly, P. S., Robinson, M. A., Rollins, A. W., Ryerson, T. B., Sekimoto, K., Thornton, J. A., Tyndall, G. S., Ullmann, K., Veres, P. R., Warneke, C., Washenfelder, R. A., Weinheimer, A. J., Wisthaler, A., Womack, C., and Brown, S. S.: Novel Analysis to Quantify Plume Crosswind Heterogeneity Applied to Biomass Burning Smoke, Environ. Sci. Technol., 55, 15646–15657, https://doi.org/10.1021/acs.est.1c03803, 2021.

Fang, Z., Deng, W., Zhang, Y., Ding, X., Tang, M., Liu, T., Hu, Q., Zhu, M., Wang, Z., Yang, W., Huang, Z., Song, W., Bi, 580 X., Chen, J., Sun, Y., George, C., and Wang, X.: Open burning of rice, corn and wheat straws: primary emissions, photochemical aging, and secondary organic aerosol formation, Atmos. Chem. Phys., 17, 14821–14839, https://doi.org/10.5194/acp-17-14821-2017, 2017.

Fioletov, V. E., McLinden, C. A., Krotkov, N., and Li, C.: Lifetimes and emissions of SO2 from point sources estimated from OMI, Geophysical Research Letters, 42, 1969–1976, https://doi.org/10.1002/2015GL063148, 2015.

585 FIREX-AQ Science Team: Fire Influence on Regional to Global Environments and Air Quality, https://doi.org/10.5067/SUBORBITAL/FIREXAQ2019/DATA001, 2019.

Fredrickson, C. D., Theys, N., and Thornton, J. A.: Satellite Evidence of HONO/NO2 Increase With Fire Radiative Power, Geophysical Research Letters, 50, e2023GL103836, https://doi.org/10.1029/2023GL103836, 2023.

Giglio, L., Randerson, J. T., and van der Werf, G. R.: Analysis of daily, monthly, and annual burned area using the fourth-590 generation global fire emissions database (GFED4): ANALYSIS OF BURNED AREA, J. Geophys. Res. Biogeosci., 118, 317–328, https://doi.org/10.1002/jgrg.20042, 2013.

Goldberg, D. L., Lu, Z., Streets, D. G., De Foy, B., Griffin, D., McLinden, C. A., Lamsal, L. N., Krotkov, N. A., and Eskes, H.: Enhanced Capabilities of TROPOMI NO2: Estimating NOx from North American Cities and Power Plants, Environ. Sci. Technol., 53, 12594–12601, https://doi.org/10.1021/acs.est.9b04488, 2019.

595 Griffin, D., McLinden, C. A., Dammers, E., Adams, C., Stockwell, C. E., Warneke, C., Bourgeois, I., Peischl, J., Ryerson, T. B., Zarzana, K. J., Rowe, J. P., Volkamer, R., Knote, C., Kille, N., Koenig, T. K., Lee, C. F., Rollins, D., Rickly, P. S., Chen, J., Fehr, L., Bourassa, A., Degenstein, D., Hayden, K., Mihele, C., Wren, S. N., Liggio, J., Akingunola, A., and Makar, P.: Biomass burning nitrogen dioxide emissions derived from space with TROPOMI: methodology and validation, Atmos. Meas. Tech., 14, 7929–7957, https://doi.org/10.5194/amt-14-7929-2021, 2021.

600 Hersbach, H., Bell, B., Berrisford, P., Biavati, G., Horányi, A., Muñoz Sabater, J., Nicolas, J., Peubey, C., Radu, R., Rozum, I., Schepers, D., Simmons, A., Soci, C., Dee, D., and Thépaut, J.: ERA5 hourly data on pressure levels from 1940 to present, https://doi.org/10.24381/cds.bd0915c6, 2023.

Jaffe, D. A. and Wigder, N. L.: Ozone production from wildfires: A critical review, Atmospheric Environment, 51, 1–10, https://doi.org/10.1016/j.atmosenv.2011.11.063, 2012.

Atmospheric
Measurement
Techniques

Discussions

605 Jin, X., Zhu, Q., and Cohen, R. C.: Direct estimates of biomass burning NOx emissions and lifetimes using daily observations from TROPOMI, Atmos. Chem. Phys., 21, 15569–15587, https://doi.org/10.5194/acp-21-15569-2021, 2021.

Joshua-Laughner and Laughner, J.: joshua-laughner/PECANS: Version 0.1.1, , https://doi.org/10.5281/ZENODO.3386651, 2023.

Judd, L., Al-Saadi, J., Szykman, J., Valin, L., Janz, S., Kowalewski, M., Eskes, H., Veefkind, J., Cede, A., Mueller, M., 610 Gebetsberger, M., Swap, R., Pierce, R., Nowlan, C., Abad, G., Nehrir, A., and Williams, D.: Evaluating Sentinel-5P TROPOMI tropospheric NO2 column densities with airborne and Pandora spectrometers near New York City and Long Island Sound, ATMOSPHERIC MEASUREMENT TECHNIQUES, 13, 6113–6140, https://doi.org/10.5194/amt-13-6113-2020, 2020.

Juncosa Calahorrano, J. F., Lindaas, J., O'Dell, K., Palm, B. B., Peng, Q., Flocke, F., Pollack, I. B., Garofalo, L. A., Farmer, 615 D. K., Pierce, J. R., Collett, J. L., Weinheimer, A., Campos, T., Hornbrook, R. S., Hall, S. R., Ullmann, K., Pothier, M. A., Apel, E. C., Permar, W., Hu, L., Hills, A. J., Montzka, D., Tyndall, G., Thornton, J. A., and Fischer, E. V.: Daytime Oxidized Reactive Nitrogen Partitioning in Western U.S. Wildfire Smoke Plumes, JGR Atmospheres, 126, https://doi.org/10.1029/2020JD033484, 2021a.

Juncosa Calahorrano, J. F., Lindaas, J., O'Dell, K., Palm, B. B., Peng, Q., Flocke, F., Pollack, I. B., Garofalo, L. A., Farmer, 620 D. K., Pierce, J. R., Collett, J. L., Weinheimer, A., Campos, T., Hornbrook, R. S., Hall, S. R., Ullmann, K., Pothier, M. A., Apel, E. C., Permar, W., Hu, L., Hills, A. J., Montzka, D., Tyndall, G., Thornton, J. A., and Fischer, E. V.: Daytime Oxidized Reactive Nitrogen Partitioning in Western U.S. Wildfire Smoke Plumes, JGR Atmospheres, 126, https://doi.org/10.1029/2020JD033484, 2021b.

Kaiser, J. W., Heil, A., Andreae, M. O., Benedetti, A., Chubarova, N., Jones, L., Morcrette, J.-J., Razinger, M., Schultz, M. 625 G., Suttie, M., and van der Werf, G. R.: Biomass burning emissions estimated with a global fire assimilation system based on observed fire radiative power, Biogeosciences, 9, 527–554, https://doi.org/10.5194/bg-9-527-2012, 2012.

Kowalewski, M. G. and Janz, S. J.: Remote sensing capabilities of the GEO-CAPE airborne simulator, SPIE Optical Engineering + Applications, San Diego, California, United States, 92181I, https://doi.org/10.1117/12.2062058, 2014.

Lamsal, L. N., Janz, S. J., Krotkov, N. A., Pickering, K. E., Spurr, R. J. D., Kowalewski, M. G., Loughner, C. P., Crawford, 630 J. H., Swartz, W. H., and Herman, J. R.: High-resolution NO2 observations from the Airborne Compact Atmospheric Mapper: Retrieval and validation, JGR Atmospheres, 122, 1953–1970, https://doi.org/10.1002/2016JD025483, 2017.

Laughner, J. L. and Cohen, R. C.: Direct observation of changing NOx lifetime in North American cities, Science, 366, 723–727, https://doi.org/10.1126/science.aax6832, 2019.

Liu, X., Zhang, Y., Huey, L. G., Yokelson, R. J., Wang, Y., Jimenez, J. L., Campuzano-Jost, P., Beyersdorf, A. J., Blake, D. 635 R., Choi, Y., St. Clair, J. M., Crounse, J. D., Day, D. A., Diskin, G. S., Fried, A., Hall, S. R., Hanisco, T. F., King, L. E., Meinardi, S., Mikoviny, T., Palm, B. B., Peischl, J., Perring, A. E., Pollack, I. B., Ryerson, T. B., Sachse, G., Schwarz, J. P., Simpson, I. J., Tanner, D. J., Thornhill, K. L., Ullmann, K., Weber, R. J., Wennberg, P. O., Wisthaler, A., Wolfe, G. M., and Ziemba, L. D.: Agricultural fires in the southeastern U.S. during SEAC [4] RS: Emissions of trace gases and particles and evolution of ozone, reactive nitrogen, and organic aerosol, JGR Atmospheres, 121, 7383–7414, 640 https://doi.org/10.1002/2016JD025040, 2016.

Liu, X., Huey, L. G., Yokelson, R. J., Selimovic, V., Simpson, I. J., Müller, M., Jimenez, J. L., Campuzano-Jost, P., Beyersdorf, A. J., Blake, D. R., Butterfield, Z., Choi, Y., Crounse, J. D., Day, D. A., Diskin, G. S., Dubey, M. K., Fortner, E., Hanisco, T. F., Hu, W., King, L. E., Kleinman, L., Meinardi, S., Mikoviny, T., Onasch, T. B., Palm, B. B., Peischl, J., Pollack, I. B., Ryerson, T. B., Sachse, G. W., Sedlacek, A. J., Shilling, J. E., Springston, S., St. Clair, J. M., Tanner, D. J.,

645 Teng, A. P., Wennberg, P. O., Wisthaler, A., and Wolfe, G. M.: Airborne measurements of western U.S. wildfire emissions: Comparison with prescribed burning and air quality implications, JGR Atmospheres, 122, 6108–6129, https://doi.org/10.1002/2016JD026315, 2017.

Lu, Z., Streets, D. G., De Foy, B., Lamsal, L. N., Duncan, B. N., and Xing, J.: Emissions of nitrogen oxides from US urban areas: estimation from Ozone Monitoring Instrument retrievals for 2005–2014, Atmos. Chem. Phys., 15, 10367–10383,
650 https://doi.org/10.5194/acp-15-10367-2015, 2015.

McLinden, C. A., Adams, C. L. F., Fioletov, V., Griffin, D., Makar, P. A., Zhao, X., Kovachik, A., Dickson, N., Brown, C., Krotkov, N., Li, C., Theys, N., Hedelt, P., and Loyola, D. G.: Inconsistencies in sulfur dioxide emissions from the Canadian oil sands and potential implications, Environ. Res. Lett., 16, 014012, https://doi.org/10.1088/1748-9326/abcbbb, 2020.

Mebust, A. K. and Cohen, R. C.: Space-based observations of fire NOx emission coefficients: a global biome-scale
655 comparison, Atmos. Chem. Phys., 14, 2509–2524, https://doi.org/10.5194/acp-14-2509-2014, 2014.

Mebust, A. K., Russell, A. R., Hudman, R. C., Valin, L. C., and Cohen, R. C.: Characterization of wildfire NOx emissions using MODIS fire radiative power and OMI tropospheric NO2 columns, Atmos. Chem. Phys., 11, 5839–5851, https://doi.org/10.5194/acp-11-5839-2011, 2011.

Palm, B. B., Peng, Q., Hall, S. R., Ullmann, K., Campos, T. L., Weinheimer, A., Montzka, D., Tyndall, G., Permar, W., Hu,
660 L., Flocke, F., Fischer, E. V., and Thornton, J. A.: Spatially Resolved Photochemistry Impacts Emissions Estimates in Fresh Wildfire Plumes, Geophysical Research Letters, 48, e2021GL095443, https://doi.org/10.1029/2021GL095443, 2021.

Paton-Walsh, C., Smith, T. E. L., Young, E. L., Griffith, D. W. T., and Guérette, É.-A.: New emission factors for Australian vegetation fires measured using open-path Fourier transform infrared spectroscopy – Part 1: Methods and Australian temperate forest fires, Atmos. Chem. Phys., 14, 11313–11333, https://doi.org/10.5194/acp-14-11313-2014, 2014.

665 Peng, Q., Palm, B. B., Melander, K. E., Lee, B. H., Hall, S. R., Ullmann, K., Campos, T., Weinheimer, A. J., Apel, E. C., Hornbrook, R. S., Hills, A. J., Montzka, D. D., Flocke, F., Hu, L., Permar, W., Wielgasz, C., Lindaas, J., Pollack, I. B., Fischer, E. V., Bertram, T. H., and Thornton, J. A.: HONO Emissions from Western U.S. Wildfires Provide Dominant Radical Source in Fresh Wildfire Smoke, Environ. Sci. Technol., 54, 5954–5963, https://doi.org/10.1021/acs.est.0c00126, 2020.

670 Plane, J. M. and Saiz-Lopez, A.: UV-Visible Differential Optical Absorption Spectroscopy (DOAS), in: Analytical Techniques for Atmospheric Measurement, edited by: Heard, D. E., Blackwell Publishing, Oxford, UK, 147–188, https://doi.org/10.1002/9780470988510.ch3, 2006.

Platt, U. and Stutz, J.: Differential Absorption Spectroscopy, in: Differential Optical Absorption Spectroscopy, Springer Berlin Heidelberg, Berlin, Heidelberg, 135–174, https://doi.org/10.1007/978-3-540-75776-4_6, 2008.

675 Santiago-De La Rosa, N., González-Cardoso, G., Figueroa-Lara, J. D. J., Gutiérrez-Arzaluz, M., Octaviano-Villasana, C., Ramírez-Hernández, I. F., and Mugica-Álvarez, V.: Emission factors of atmospheric and climatic pollutants from crop residues burning, Journal of the Air & Waste Management Association, 68, 849–865, https://doi.org/10.1080/10962247.2018.1459326, 2018.

Schmidt, C.: Monitoring Fires with the GOES-R Series, in: The GOES-R Series, Elsevier, 145–163,
680 https://doi.org/10.1016/B978-0-12-814327-8.00013-5, 2020.

Atmospheric
Measurement
Techniques
Discussions

Schreier, S. F., Richter, A., Kaiser, J. W., and Burrows, J. P.: The empirical relationship between satellite-derived tropospheric NO2 and fire radiative power and possible implications for fire emission rates of NOx, Atmos. Chem. Phys., 14, 2447–2466, https://doi.org/10.5194/acp-14-2447-2014, 2014.

685 Schreier, S. F., Richter, A., Schepaschenko, D., Shvidenko, A., Hilboll, A., and Burrows, J. P.: Differences in satellite-derived NOx emission factors between Eurasian and North American boreal forest fires, Atmospheric Environment, 121, 55–65, https://doi.org/10.1016/j.atmosenv.2014.08.071, 2015.

Solomon, S., Dube, K., Stone, K., Yu, P., Kinnison, D., Toon, O. B., Strahan, S. E., Rosenlof, K. H., Portmann, R., Davis, S., Randel, W., Bernath, P., Boone, C., Bardeen, C. G., Bourassa, A., Zawada, D., and Degenstein, D.: On the stratospheric chemistry of midlatitude wildfire smoke, Proc. Natl. Acad. Sci. U.S.A., 119, e2117325119, 690 https://doi.org/10.1073/pnas.2117325119, 2022.

Solomon, S., Stone, K., Yu, P., Murphy, D. M., Kinnison, D., Ravishankara, A. R., and Wang, P.: Chlorine activation and enhanced ozone depletion induced by wildfire aerosol, Nature, 615, 259–264, https://doi.org/10.1038/s41586-022-05683-0, 2023.

Stockwell, C. E., Veres, P. R., Williams, J., and Yokelson, R. J.: Characterization of biomass burning emissions from 695 cooking fires, peat, crop residue, and other fuels with high-resolution proton-transfer-reaction time-of-flight mass spectrometry, Atmos. Chem. Phys., 15, 845–865, https://doi.org/10.5194/acp-15-845-2015, 2015.

Takegawa, N., Kondo, Y., Koike, M., Ko, M., Kita, K., Blake, D. R., Nishi, N., Hu, W., Liley, J. B., Kawakami, S., Shirai, T., Miyazaki, Y., Ikeda, H., Russel-Smith, J., and Ogawa, T.: Removal of NOx and NOy in biomass burning plumes in the boundary layer over northern Australia, J. Geophys. Res., 108, 2002JD002505, https://doi.org/10.1029/2002JD002505, 700 2003.

Tanimoto, H., Ikeda, K., Folkert Boersma, K., Van Der A, R. J., and Garivait, S.: Interannual variability of nitrogen oxides emissions from boreal fires in Siberia and Alaska during 1996–2011 as observed from space, Environ. Res. Lett., 10, 065004, https://doi.org/10.1088/1748-9326/10/6/065004, 2015.

Theys, N., Volkamer, R., Müller, J.-F., Zarzana, K. J., Kille, N., Clarisse, L., De Smedt, I., Lerot, C., Finkenzeller, H., 705 Hendrick, F., Koenig, T. K., Lee, C. F., Knote, C., Yu, H., and Van Roozendael, M.: Global nitrous acid emissions and levels of regional oxidants enhanced by wildfires, Nat. Geosci., 13, 681–686, https://doi.org/10.1038/s41561-020-0637-7, 2020.

Urbanski, S.: Wildland fire emissions, carbon, and climate: Emission factors, Forest Ecology and Management, 317, 51–60, https://doi.org/10.1016/j.foreco.2013.05.045, 2014.

710 Wang, S., Coggon, M. M., Gkatzelis, G. I., Warneke, C., Bourgeois, I., Ryerson, T., Peischl, J., Veres, P. R., Neuman, J. A., Hair, J., Shingler, T., Fenn, M., Diskin, G., Huey, L. G., Lee, Y. R., Apel, E. C., Hornbrook, R. S., Hills, A. J., Hall, S. R., Ullmann, K., Bela, M. M., Trainer, M. K., Kumar, R., Orlando, J. J., Flocke, F. M., and Emmons, L. K.: Chemical Tomography in a Fresh Wildland Fire Plume: A Large Eddy Simulation (LES) Study, JGR Atmospheres, 126, https://doi.org/10.1029/2021JD035203, 2021.

715 van der Werf, G. R., Randerson, J. T., Giglio, L., van Leeuwen, T. T., Chen, Y., Rogers, B. M., Mu, M., van Marle, M. J. E., Morton, D. C., Collatz, G. J., Yokelson, R. J., and Kasibhatla, P. S.: Global fire emissions estimates during 1997-2016, Earth Syst. Sci. Data, 9, 697–720, https://doi.org/10.5194/essd-9-697-2017, 2017.

Wiedinmyer, C. and Emmons, L.: Fire Inventory from NCAR version 2 Fire Emission, https://doi.org/10.5065/XNPA-AF09, 2022.

720 Wiedinmyer, C., Akagi, S. K., Yokelson, R. J., Emmons, L. K., Al-Saadi, J. A., Orlando, J. J., and Soja, A. J.: The Fire INventory from NCAR (FINN): a high resolution global model to estimate the emissions from open burning, Geosci. Model Dev., 4, 625–641, https://doi.org/10.5194/gmd-4-625-2011, 2011.

Wiedinmyer, C., Kimura, Y., McDonald-Buller, E. C., Emmons, L. K., Buchholz, R. R., Tang, W., Seto, K., Joseph, M. B., Barsanti, K. C., Carlton, A. G., and Yokelson, R.: The Fire Inventory from NCAR version 2.5: an updated global fire 725 emissions model for climate and chemistry applications, Geosci. Model Dev., 16, 3873–3891, https://doi.org/10.5194/gmd-16-3873-2023, 2023.

Wiggins, E. B., Soja, A. J., Gargulinski, E., Halliday, H. S., Pierce, R. B., Schmidt, C. C., Nowak, J. B., DiGangi, J. P., Diskin, G. S., Katich, J. M., Perring, A. E., Schwarz, J. P., Anderson, B. E., Chen, G., Crosbie, E. C., Jordan, C., Robinson, C. E., Sanchez, K. J., Shingler, T. J., Shook, M., Thornhill, K. L., Winstead, E. L., Ziemba, L. D., and Moore, R. H.: High 730 Temporal Resolution Satellite Observations of Fire Radiative Power Reveal Link Between Fire Behavior and Aerosol and Gas Emissions, Geophys. Res. Lett., 47, https://doi.org/10.1029/2020GL090707, 2020.

Wolfe, G. M., Hanisco, T. F., Arkinson, H. L., Blake, D. R., Wisthaler, A., Mikoviny, T., Ryerson, T. B., Pollack, I., Peischl, J., Wennberg, P. O., Crounse, J. D., St. Clair, J. M., Teng, A., Huey, L. G., Liu, X., Fried, A., Weibring, P., Richter, D., Walega, J., Hall, S. R., Ullmann, K., Jimenez, J. L., Campuzano-Jost, P., Bui, T. P., Diskin, G., Podolske, J. R., Sachse, G., 735 and Cohen, R. C.: Photochemical evolution of the 2013 California Rim Fire: synergistic impacts of reactive hydrocarbons and enhanced oxidants, Atmos. Chem. Phys., 22, 4253–4275, https://doi.org/10.5194/acp-22-4253-2022, 2022.

Xue, R., Wang, S., Zhang, S., He, S., Liu, J., Tanvir, A., and Zhou, B.: Estimating city NOX emissions from TROPOMI high spatial resolution observations – A case study on Yangtze River Delta, China, Urban Climate, 43, 101150, https://doi.org/10.1016/j.uclim.2022.101150, 2022.

740 Ye, X., Arab, P., Ahmadov, R., James, E., Grell, G. A., Pierce, B., Kumar, A., Makar, P., Chen, J., Davignon, D., Carmichael, G. R., Ferrada, G., McQueen, J., Huang, J., Kumar, R., Emmons, L., Herron-Thorpe, F. L., Parrington, M., Engelen, R., Peuch, V.-H., Da Silva, A., Soja, A., Gargulinski, E., Wiggins, E., Hair, J. W., Fenn, M., Shingler, T., Kondragunta, S., Lyapustin, A., Wang, Y., Holben, B., Giles, D. M., and Saide, P. E.: Evaluation and intercomparison of wildfire smoke forecasts from multiple modeling systems for the 2019 Williams Flats fire, Atmos. Chem. Phys., 21, 14427–745 14469, https://doi.org/10.5194/acp-21-14427-2021, 2021.